

XMM-Newton Observations of Two Candidate Supernova Remnants¹

O. Kargaltsev¹, B. M. Schmitt², G. G. Pavlov^{2,3}, Z. Misanovic⁴

¹*Dept. of Astronomy, University of Florida, Gainesville, FL 32611-2055, USA*

²*Dept. of Astronomy and Astrophysics, The Pennsylvania State University,
525 Davey Lab., University Park, PA 16802*

³*St. Petersburg State Polytechnical University, Polytechnicheskaya ul. 29, St. Petersburg
195251, Russia*

⁴*School of Physics, Monash University, Melbourne, 3800 VIC, Australia*

ABSTRACT

Candidate supernova remnants G23.5+0.1 and G25.5+0.0 were observed by *XMM-Newton* in the course of a snap-shot survey of plerionic and composite SNRs in the Galactic plane. In the field of G23.5+0.1, we detected an extended source, $\sim 3'$ in diameter, which we tentatively interpret as a pulsar-wind nebula (PWN) of the middle-aged radio pulsar B1830–08 (J1833–0827; $P = 85.3$ ms, $\tau = 147$ kyr, $\dot{E} = 5.8 \times 10^{35}$ erg s^{−1}, $d = 5.7$ kpc), with the PWN luminosity $L_{0.2-10\text{ keV}} \approx 5 \times 10^{33}$ erg s^{−1} $\approx 8 \times 10^{-3} \dot{E}$. The pulsar is not resolved in the EPIC images. Our analysis suggests an association between PSR B1830–08 and the surrounding diffuse radio emission. If the radio emission is due to the SNR, then the pulsar must be significantly younger than its characteristic age. Alternatively, the radio emission may come from a relic PWN. The field also contains SGR 1833–0832 and another middle-aged pulsar B1829–08 [J1832–0827; $P = 647$ ms, $\tau = 161$ kyr, $\dot{E} = 9.3 \times 10^{33}$ erg s^{−1}, $d = 4.7$ kpc], none of which are detected in our observation. In the field of G25.5+0.0, which contains the extended TeV source HESS J1837–069, we detected the recently discovered young high-energy pulsar J1838–0655 ($P = 70.5$ ms, $\tau = 23$ kyr, $\dot{E} = 5.5 \times 10^{36}$ erg s^{−1}) embedded in a PWN with extent of $1.3'$. The unabsorbed pulsar + PWN luminosity is $L_{2-11\text{ keV}} \approx 2 \times 10^{34}$ erg s^{−1} $\approx 4 \times 10^{-3} \dot{E}$ at an assumed distance of 7 kpc. We also detected another PWN candidate (AX J1837.3–0652) with an extent of $2'$ and unabsorbed luminosity $L_{2-10\text{ keV}} \approx 4 \times 10^{33}$ erg s^{−1} at $d = 7$ kpc. The third X-ray source, located within the extent of the HESS J1837–069, has a peculiar extended radio counterpart, possibly a radio galaxy with a double nucleus or a microquasar. We did not find any evidence of the SNR emission in the G25.5+0.0 field. We provide detailed multiwavelength analysis

and identifications of other field sources and discuss robustness of the G25.5+0.0 and G23.5+0.1 classifications as SNRs.

Subject headings: SNR: individual (G23.5+0.1, G25.5+0.0, AX J1838.0–065, AX J1838.3–062) — ISM: individual (HESS J1809–193) – pulsars: individual (PSR B1829–08, PSR B1830–08, PSR J1838–0655) — stars: neutron: individual (SGR 1833-0832) — stars: neutron — X-rays: ISM

1. Introduction

Modern X-ray observatories are powerful tools for studying diffuse emission in crowded regions of the Galactic plane. The diffuse X-ray emission is often associated with the end products of stellar evolution such as supernova remnants (SNRs) and young pulsars (PSRs) enveloped by pulsar wind nebulae (PWNe). Although growing, the number of SNRs and pulsars found in X-ray data is still significantly smaller than the corresponding numbers of detections in the radio. For instance, only about 100 out of ~ 1900 non-recycled, rotation-powered radio pulsars have been detected in X-rays. Similarly, the number of known radio SNRs stands at 274 (Green 2009), while the number of Galactic SNRs detected in X-rays is about 50 (e.g., Seward et al. 2010). Therefore, further detections of SNRs and PSRs/PWNe in X-rays would be a valuable addition to the existing limited sample. However, detecting and identifying sources of diffuse X-ray emission in the Galactic plane is often challenging because of the large intervening absorption column and scores of background/foreground point sources. For instance, it is very likely that among 20,837 extended emission detections in the Second *XMM-Newton* Serendipitous Source Catalogue (2XMM²) there are quite a few SNRs and PWNe, yet many of them could not be identified/classified automatically based solely on X-ray data. A thorough multiwavelength analysis is often required to understand the nature of the observed extended X-ray emission. To expand the current sample of X-ray observed pulsars and PWNe and establish the characteristics of the population as a whole, we have conducted an *XMM-Newton* survey of 14 plerionic and composite SNRs or SNR candidates within an 8 kpc distance. First results have been presented by Misanovic et al. (2010). Here we report the results of our *XMM-Newton* observations of two SNR candidates from that sample: G23.5+0.1 and G25.5–0.0.

¹Based on observations obtained with XMM-Newton, an ESA science mission with instruments and contributions directly funded by ESA Member States and NASA.

²See http://xmssc-www.star.le.ac.uk/Catalogue/xcatalog_public_2XMM.html

G23.5+0.1 is a candidate SNR discovered in a 19 ks *ASCA* observation carried out as part of the Galactic plane survey (Yamauchi et al. 2002). A radio pulsar, B1830–08 (also known as PSR J1833–0827) is located at $l = 23.386^\circ$, $b = 0.063^\circ$, close to the center of the diffuse X-ray emission seen in the *ASCA* image (Ueno 2005). It is a middle-aged ($\tau \equiv P/2\dot{P} = 148$ kyr), 85 ms pulsar at a distance³ of about 5.7 kpc, with a spin-down energy loss rate $\dot{E} = 5.8 \times 10^{35}$ erg s^{−1}. The pulsar is known to exhibit strong glitches (Hobbs et al. 2004), and it has the proper motion of 34 ± 6 mas yr^{−1} toward the Galactic north, away from the Galactic plane (Hobbs et al. 2005). Located nearby ($\sim 24'$ southeast) are the radio-bright shell SNR W41 (G23.3–0.3) and an extended TeV source HESS J1834–087 (with a radial extent of $\sim 5.4'$) projected within the shell. Clifton & Lyne (1986) mentioned W41 as a possible host SNR to PSR B1830–08. Gaensler & Johnston (1995) also attempted to associate the pulsar with W41, but concluded that the pulsar’s age does not agree with the age of the remnant. Aharonian et al. (2006) discussed a possible relation between HESS J1834–087, W41, and PSR B1830–08 and suggested a “compelling positional agreement” between HESS J1834–087 and W41. However, the large separation between PSR B1830–08 and HESS J1834–087 made the association questionable (Aharonian et al. 2006). More likely, PSR B1830–08 could be associated with G23.5+0.1 if it is indeed an SNR. Another middle-aged pulsar, B1829–08 (also known as J1832–0827; $P = 647$ ms, $\tau = 161$ kyr, $d \sim 4.7$ kpc), with a rather low $\dot{E} = 9.3 \times 10^{33}$ erg s^{−1}, is located $\sim 16'$ southwest of G23.5+0.1. There may also be a compact TeV source, HESS J1832–084 (*Suzaku* AO-5 program, ObsID 506021010; PI G. Püehlhofer), spatially coincident but not necessarily associated with this pulsar. Finally, the field also contains a recently discovered Soft Gamma Repeater, SGR J1833–0832 (Gelbord et al. 2010).

G25.5+0.0 was detected with *ASCA* as an extended X-ray source (AX J1838.0–065) and classified as a possible non-thermal SNR by Bamba et al. (2003), who estimated the distance and diameter to be 7.8 kpc and 27 pc, respectively. The TeV source HESS J1837–069 was found within the extent of the G25.5+0.0 SNR candidate (Aharonian et al. 2006). Subsequently, Gotthelf & Halpern (2008; hereafter GH08) studied possible association between HESS J1837–069 and AX J1838.0–065 using *RXTE* and archival *Chandra* data. The analysis of the *Chandra* ACIS images revealed two extended X-ray sources: one coincident with the aforementioned AX J1838.0–065, and the other (fainter and more extended) coincident with another *ASCA* source, AX J1838.3–062. Both sources were found to be relatively close to the HESS source position; however, only AX J1838.0–065 fell within the 1σ extent of the TeV emission. Timing analysis of the *RXTE* data revealed a 70.5 ms, young ($\tau = 23$ kyr)

³Here and below the pulsar distances are inferred from the pulsar’s dispersion measure (DM) and the model of Galactic electron density by Taylor & Cordes (1993).

and powerful ($\dot{E} = 5.5 \times 10^{36}$ erg s $^{-1}$) pulsar J1838–0655 in the core of AX J1838.0–065, thus solidifying the association between AX J1838.0–065 and the HESS source. Spectral analysis of the *Chandra* ACIS data revealed an unusually hard, strongly absorbed spectrum (photon index $\Gamma = 0.7 \pm 0.2$, $N_H = (4.5 \pm 0.75) \times 10^{22}$ cm $^{-2}$, for the absorbed power-law (PL) model). The *Chandra* images also showed that the pulsar is accompanied by a PWN of a comparable luminosity, with a much softer spectrum ($\Gamma = 1.6 \pm 0.45$). GH08 noticed that although PSR J1838–0655 is an obvious counterpart to HESS J1837–069, the source AX J1838.3–062, tentatively classified as a candidate PWN, could also contribute to the TeV emission seen from HESS J1837–069. Spectral analysis of the ACIS data on AX J1838.3–062 gave poorly constrained parameters: $0.7 < \Gamma < 3.6$ and $N_H = (7 \pm 5) \times 10^{22}$ cm $^{-2}$, for the absorbed PL model fit.

Here we present an analysis of *XMM-Newton* observations of these two SNR candidate fields rich with interesting high-energy sources. In Section 2 we describe the observations. Section 3 provides a summary of the data analysis and source detection techniques and describes the properties of the detected X-ray sources. In Section 4 we discuss the classification of the detected X-ray sources, based on optical, near-infrared, and high-energy data. Finally, we discuss the pulsar/PWN candidates detected in our observations in Section 5 and summarize our conclusions in Section 6.

2. Observations

The fields of the SNR candidates G23.5+0.1 and G25.5+00 were observed with the *XMM-Newton* EPIC PN and MOS detectors in Full Frame mode with Medium filter. This mode offers the time resolution of 73.4 ms for PN and 2.6 s for MOS. The G23.5+0.1 field was observed in a single pointing, while the G25.5+0.0 field was covered with two pointings (with a 9′ offset). Additional details of these observations are listed in Table 1. There were no strong background ares during these observations.

3. Source Detection and Data Analysis

The data were reduced and analyzed using the *XMM-Newton* Science Analysis System (SAS), ver. 8.0.1. Calibrated event files for the PN, MOS1, and MOS2 detectors were produced using the SAS tasks *epchain* and *emchain*, following standard procedures. To search for X-ray sources and extract their properties, we used the SAS task *edetect_chain*. This task runs on the event lists and invokes several other SAS tasks to produce background,

sensitivity, and vignetting-corrected exposure maps. Three image sets (one per detector), three event lists (one per detector), and a user-defined likelihood threshold parameter *mlmin* for each of the fields were used as inputs. In both fields we set the *mlmin* parameter to 7, corresponding to a $\simeq 4\sigma$ detection.

In addition, we produced combined (mosaicked) PN, MOS1, and MOS2 images (using the SAS task *emosaic*), smoothed with a gaussian kernel ($r = 24''$). We visually inspected the combined, smoothed images to look for faint extended emission, which may not be detected automatically by *edetect_chain* because of algorithm limitations.

Since the fields of view (FOV) of the two observations of G25.5+0.0 are partly overlapping, we searched for X-ray sources in each of the two pointings as well as in the combined data. This allowed us to look for a long term variability of the sources located in the overlapping region.

Given the short exposure times, spectral analysis is warranted only for relatively bright sources. We chose the signal-to-noise (S/N) ratios of 25 and 10 as thresholds for point and diffuse sources, respectively. There are only two sources (1 and 8) in the G23.5+0.1 field and four sources (1, 6, 7, and 15) in the G25.5+0.0 field that meet this requirement. The SAS spectral extraction metatask *especget* invokes several other tasks to produce the source spectra, background spectra, response files, and effective area files. We maximized the S/N by extracting spectra from all the detectors whenever possible. The spectra were binned and then fitted with XSPEC (ver. 12.4.0ad). Two spectral models were used to fit the spectra: the optically-thin thermal plasma emission model (*mekal*) was used for soft sources (in which most of the emission is at energies $\lesssim 3$ keV), while the PL model was used for sources exhibiting harder spectra. For each source we quote the measured, absorbed fluxes (based on the best-fit model) for the energy ranges where there are enough counts. We also used the XSPEC task *cflux* to estimate unabsorbed X-ray fluxes (see Tables 4 and 5).

Keeping in mind that most sources are too faint for spectral fitting, we crudely estimated their X-ray fluxes from count rates using the same energy conversion factors (ECFs) as in the 2XMM catalog⁴, which were calculated for an absorbed PL spectrum with $\Gamma = 1.7$ and $N_H = 3 \times 10^{20} \text{ cm}^{-2}$. The low N_H is appropriate for about 30% of the detected sources (which are likely to be nearby foreground stars, see below) while other sources likely to have larger N_H varying significantly from source to source. Therefore, for some heavily absorbed sources the fluxes provided in Tables 2 and 3 may overestimate the actual flux by up to a factor of 3. However, we use these fluxes solely for source classification purposes and our classification scheme is rather insensitive to X-ray flux variations at such a level (see §5 and

⁴See http://xmmssc-www.star.le.ac.uk/Catalogue/2XMM/UserGuide_xmmcat.html#EmldetFit

Fig. 7). For several bright sources we perform the actual spectral fits and provide accurate fluxes (see below), which differ from those in Tables 2 and 3 by up to a factor of 3 due to a the pre-defined, fixed model being used in calculating the ECFs. For each source we also estimated the hardness ratio,

$$\text{HR} = (f_{2-12} - f_{0.2-2}) / (f_{2-12} + f_{0.2-2}), \quad (1)$$

where $f_{0.2-2}$ and f_{2-12} are the observed (absorbed) fluxes in the 0.2–2 and 2–12 keV bands, respectively. The hardness ratios given in Tables 2 and 3 are used for source classification together with the multiwavelength properties.

3.1. G23.5+0.1 field

Excluding spurious sources along the chip gaps and bad columns, the *edetect_chain* task detected 7 sources in the G23.5+0.1 field. These sources are listed in Table 2 and shown in Figure 1. All the automatically detected sources in the G23.5+0.1 field appear to be point sources. In addition, by visual inspection we found a region of diffuse X-ray emission (labeled Source 8) at the center of the G23.5+0.1 field (see Figure 1). Source 8 was not automatically detected (the detection algorithm is not sensitive to faint diffuse sources having large extent), but the diffuse emission, mostly confined within a $2'$ radius region, is clearly visible, especially in the smoothed image (Figure 1, middle).

3.1.1. Spectral fits for brighter sources

Source 1: The spectrum was extracted from a $20''$ radius aperture, for the PN, MOS1, and MOS2, resulting in ≈ 1200 combined, background-subtracted counts. The background spectrum was extracted from a nearby circular region of $80''$ radius. The counts were grouped in 65 PN, 23 MOS1, and 19 MOS2 energy bins with about 20 total counts per bin. The spectrum does not fit the absorbed PL model but fits well the absorbed *mekal* model with $kT = 0.6 \pm 0.2$ keV and $N_H = (1.3 \pm 0.2) \times 10^{21} \text{ cm}^{-2}$ ($\chi^2_\nu = 1.2$ for 71 degrees of freedom [d.o.f., hereafter]), suggesting X-ray emission from a foreground star (see Section 4). The observed (absorbed) X-ray flux in the 0.3–5 keV is $f_{0.3-5} = (1.8 \pm 0.1) \times 10^{-13} \text{ erg s}^{-1} \text{ cm}^{-2}$. The detailed results of the spectral fitting are given in Table 4, and the fit is shown in Figure 3.

Source 8: The spectrum of the extended emission at the center of G23.5+0.1 (Source 8 in Figure 1) was extracted from a circular aperture with the radius of $70''$ from the PN, MOS1, and MOS2 images. This gave 1565 combined, background-subtracted counts (background

contribution $\simeq 35\%$). The background spectrum was extracted from a nearby circular region of the $80''$ radius. The counts were grouped in 20 PN, 22 MOS1, and 22 MOS2 energy bins with about 70 total counts per bin in PN and 22 total counts in MOS1 and 2. The spectrum fits best the absorbed PL model ($\chi^2_\nu = 1.3$ for 48 d.o.f) with photon index $\Gamma = 2.3 \pm 0.8$ and $N_H = (3.9 \pm 1.9) \times 10^{22} \text{ cm}^{-2}$. The large hardness ratio, $\text{HR} = 0.9 \pm 0.1$, reflects the fact that the source is very strongly absorbed even though it has a rather soft spectrum. The observed absorbed X-ray flux in the 1–10 keV band is $f_{1-10} = (2.0 \pm 0.3) \times 10^{-13} \text{ erg s}^{-1} \text{ cm}^{-2}$. The detailed results of the spectral fitting are given in Table 5, and the fit is shown in Figure 4. We have also analyzed archived data from an 8 ks *Chandra* ACIS observation of the G23.5+0.1 field (PI B. Gaensler; ObsID 10524). In the ACIS-S3 image (see the inset in Fig. 1, middle panel) we found a region of faint diffuse emission and a point source, CXOU J183340.3–082830 (located $\approx 58''$ north of the radio position of PSR B1830–08), both of which are located within the extent of the diffuse Source 8.

3.1.2. Upper limits on undetected sources

As we did not detect X-ray emission from PSR B1830–08, PSR B1829–08, and SGR J1833–0832, we can only estimate upper limits on their fluxes. The upper limit on the flux depends on the assumed spectral shape. Spectra of middle-aged pulsars, such as B1830–08 and B1829–08, can be usually described by a sum of PL and blackbody components. Taking as a proxy the spectrum of the nearby middle-aged ($\tau = 110 \text{ kyr}$) pulsar B0656+14 (De Luca et al. 2005), with the hydrogen column density changed from 4×10^{20} to $3 \times 10^{22} \text{ cm}^{-2}$, we obtained upper limits of 4×10^{-14} and $3 \times 10^{-14} \text{ ergs s}^{-1} \text{ cm}^{-2}$ (at 90% confidence) on the observed flux in the 0.2–10 keV band for PSR B1830–08 and PSR B1829–08, respectively⁵. Similar upper limits are obtained assuming an absorbed PL model with $\Gamma = 2$ and the same N_H . The upper limits on the unabsorbed fluxes are 6×10^{-13} and $4 \times 10^{-13} \text{ ergs s}^{-1} \text{ cm}^{-2}$, respectively.

SGR J1833–0832 was in a quiescent state during our observation. It is not obvious which spectral model should be assumed for a magnetar in a quiescent state because the spectra are different in different sources, and, apparently, some quiescent magnetars are simply too dim to measure their spectra. If the best-fit spectral model⁶ of the transient magnetar XTE

⁵The limits, estimated with PIMMS; <http://heasarc.gsfc.nasa.gov/Tools/w3pimms.html>, taking vignetting into account.

⁶A two-component black-body with $kT_{\text{cold}} \approx 167 \text{ eV}$, $R_{\text{cold}} \approx 9.3 \text{ km}$, $kT_{\text{hot}} \approx 330 \text{ eV}$, and $R_{\text{hot}} \approx 0.9 \text{ km}$ (see Table 3 in Bernardini et al. 2009).

J1810–197 in its lowest flux state (2007 September) is taken as a proxy, an upper limit $f_{0.2-10} < 6 \times 10^{-15}$ ergs s^{−1} cm^{−2} (at 90% confidence in 0.2–10 keV) on the flux of SGR J1833–0832 is obtained (the corresponding unabsorbed flux is $f_{0.2-10}^{\text{unabs}} \lesssim 1.6 \times 10^{-13}$ ergs s^{−1} cm^{−2} for $N_H = 3 \times 10^{22}$ cm^{−2}, close to that estimated by Esposito et al. 2011). If, instead, the spectrum of the quiescent SGR 0526–66 is taken as a proxy (PL with $\Gamma = 3.3$; Tiengo et al. 2009), we obtain similar limits: $f_{0.2-10} \lesssim 5 \times 10^{-15}$ ergs s^{−1} cm^{−2} and $f_{0.2-10}^{\text{unabs}} \lesssim 1.4 \times 10^{-13}$ ergs s^{−1} cm^{−2}, again assuming $N_H = 3 \times 10^{22}$ cm^{−2}. We note that these estimates are approximate and may vary by a factor of a few depending on the actual spectrum of SGR J1833–0832 in quiescence. The reason the limits are shallower for the pulsars compared to SGR J1833–0832 is that PSR B1830–08 is located within the enhanced diffuse emission region, and PSR B1829–08 is near the edge of the EPIC FOV (see Figure 1), where the sensitivity is a factor of 2.5 lower. Note, however, that the fits to the SGR J1833–0832 spectrum in its active state indicate an absorbing column $N_H = (1.0\text{--}1.6) \times 10^{23}$ cm^{−2} (Gögüş et al. 2010), which is an order of magnitude higher than the total HI column in that direction (1.7×10^{22} cm^{−2}). If this extra absorption is not intrinsic to the active state, then the source must be located behind a very dense, cold molecular cloud, in which case the upper limit on the absorbed flux would go up by a factor of 2–2.5 (more for the unabsorbed flux limit), thus bringing it close to the 3.4×10^{-13} erg s^{−1} cm^{−2} upper limit reported by Gögüş et al. (2010) from the 8 ks *Chandra* ACIS observation.

3.2. G25.5+0.0 field

Automated *edetect_chain* detection procedure reported 23 reliable detections (excluding spurious detections along the chip gaps and bad columns). These sources are shown in Figure 2 and listed in Table 3. Among these sources seven were within the FOV of both pointings (these sources are marked with an asterisk in Table 3 and throughout the text).

Three sources (1, 6, 15) were flagged as extended by the *edetect_chain* detection procedure, which we confirmed by visual inspection. Source 1, the brightest X-ray source in the field, is located within the 1σ extent of the TeV source HESS J1837–069 (see Fig. 21 in Aharonian et al. 2006). Source 6 is either diffuse or multiple (see below). Extended Source 15 appears to be elongated along the North-South axis on arcminute scale. A smoothed, mosaicked, and vignetting-corrected image (Figure 2, middle panel) was examined for additional sources of extended emission. Upon visual inspection, we found an extended ($\sim 4'$ in diameter) partial shell of faint emission near the western boundary of the FOV (indicated by a yellow ellipse in Figure 2), which could be either truly diffuse or produced by multiple faint point sources clustered in a circular shape.

We note that several additional point sources, which were neither apparent in separate MOS/PN images nor detected automatically, are seen in the combined, smoothed image. Since these sources are faint, little information can be extracted from the existing data even if some of these sources are real. Therefore, we do not include these sources in any of the tables and do not discuss them below.

3.2.1. Spectral fits for brighter sources

Source 1: The position of the extended Source 1 coincides with the position of AX J1838.0–065, detected in *Chandra* data and identified as PSR J1838–0655 with a PWN resolved out to $\simeq 40''$ – $50''$ from the pulsar (GH08). According to *edetect_chain*, the radial extent of the source is $\simeq 30''$. As this source happens to be outside the FOV of the PN and MOS1 detectors, the spectral extraction was only possible from the MOS2 detector (and only in one of the two pointings), resulting in ~ 660 background-subtracted counts in a $40''$ radius aperture. The background spectrum was extracted from a nearby circular region with the radius of $80''$. The counts were grouped into 50 energy bins with about 15 counts per bin. We found the best-fit model to be an absorbed PL ($\chi^2_\nu = 0.7$ for 41 d.o.f.) with $\Gamma = 1.25^{+0.30}_{-0.14}$ and $N_H = 5.2^{+1.0}_{-0.8} \times 10^{22} \text{ cm}^{-2}$. The fit is in agreement with the analysis of GH08, although our estimated absorption column seems to be slightly higher (GH08 found $N_H = 4.5^{+0.7}_{-0.8} \times 10^{22} \text{ cm}^{-2}$). For the PWN, GH08 measured $\Gamma = 1.6^{+0.4}_{-0.5}$ from the *Chandra* ACIS data, which is almost the same as the value we found from the PSR+compact PWN (up to $r = 40''$). The observed X-ray flux in the 1–11 keV band is $f_{1-11} = (5.4 \pm 0.4) \times 10^{-12} \text{ erg s}^{-1} \text{ cm}^{-2}$. The detailed results of spectral fitting are given in Table 5 and the fit is shown in Figure 4.

Source 6: This source appears to be marginally extended (radial extent $r = 11''$ as determined by *edetect_chain*). However, *Chandra* resolved this source into three point source which are smeared out in the EPIC images because of the broader PSF of *XMM-Newton*. As the sources coincide with the young ($\simeq 1 \text{ Myr}$), strongly obscured, dense (core diameter $\simeq 20''$) star-forming region W42 (Blum et al. 2000), the detected emission is likely to come from magnetically active and/or pre-main-sequence (PMS) stars. The spectrum of Source 6 was extracted from the PN, MOS1, and MOS2 detectors with ≈ 400 combined, background-subtracted counts in an $r = 33''$ circular aperture. The background spectrum was extracted from a nearby circular region with $r = 80''$. Counts were grouped in 22 PN, 9 MOS1, and 9 MOS2 energy bins with 13–15 total counts per bin. We fitted the Source 6 spectrum with the absorbed *mekal* and PL models, and found that the *mekal* model fits better ($\chi^2_\nu = 1.05$ vs. $\chi^2_\nu = 1.31$ for the PL model, for 52 d.o.f.). The best-fit model implies a high temperature,

$kT = 2.2_{-0.3}^{+0.4}$ keV, and large $N_H = (2.8 \pm 0.4) \times 10^{22} \text{ cm}^{-2}$, consistent with the large extinction found toward W42 ($A_V \sim 32$; Blum et al. 2000). The observed X-ray flux in the 1–8 keV band is $f_{1-8} = (3.6 \pm 0.2) \times 10^{-13} \text{ erg s}^{-1} \text{ cm}^{-2}$. Additional details on spectral fitting are given in Tables 4 and 5, and the fits are shown in Figures 3 and 4.

*Source 7**: The spectrum was extracted from the PN detector only (due to a low S/N ratio for the MOS data), with ~ 340 background-subtracted counts in a circular aperture with $r = 20''$. The background spectrum was extracted from a nearby region with an $80''$ radius. The counts were grouped into 21 energy bins with about 19 total counts per bin. The best-fit model is an absorbed *mekal* ($\chi^2_\nu = 0.99$ for 21 d.o.f) with $kT = 0.28 \pm 0.07$ keV and $N_H = 3.8_{-0.5}^{+1.7} \times 10^{21} \text{ cm}^{-2}$. The observed X-ray flux in the 0.3–2 keV band is $f_{0.3-2} = (6.5 \pm 0.5) \times 10^{-14} \text{ erg s}^{-1} \text{ cm}^{-2}$. The details of the spectral fit are provided in Table 4 and the spectrum is shown in Figure 4.

Source 15: This source coincides with the PWN candidate AX J1838.3–062 (GH08). It appears to be extended, with the radial extent of $\approx 20''$ (according to *edetect_chain*). A very faint arcminute-scale emission is seen upon visual inspection in the smoothed combined PN image. The spectrum, extracted from the PN, MOS1, and MOS2 detectors, has $\simeq 250$ combined, background-subtracted counts in a circular aperture with $r = 60''$. The background spectrum was extracted from a nearby circular region with $r = 80''$. Counts were grouped into 20 PN, 11 MOS1, and 11 MOS2 energy bins, with 13–14 and 6–8 total counts per bin for PN and MOS1/2, respectively. The spectrum fits best an absorbed PL model ($\chi^2_\nu = 0.95$ for 45 d.o.f) with $\Gamma = 2.1_{-0.6}^{+0.9}$ and $N_H = 6.7_{-2.2}^{+3.8} \times 10^{22} \text{ cm}^{-2}$. Thus, our fit is better constrained than that reported by GH08 (see also Section 1). The observed X-ray flux in the 2–10 keV band is $f_{2-10} = (3.7 \pm 0.9) \times 10^{-13} \text{ erg s}^{-1} \text{ cm}^{-2}$. As noted by GH08, the spectrum of this source is probably dominated by the nebular emission. The complete results of the spectral fitting are given in Table 5, while the spectrum and the fit are shown in Figure 4.

4. Multiwavelength Analysis

We use the positions of the reliably detected X-ray sources (Tables 2 and 3) to perform multiwavelength cross-correlation and analysis. We carried out the cross-correlation search with the following catalogs: MAGPIS (White et al. 2005), NVSS (Condon et al. 1998), and ATNF Pulsar Catalog (Manchester et al. 2005) in the radio; 2MASS (Skrutskie et al. 2006), USNO-B1.0 (Monet et al. 2003)], and *HST* Guide Star Catalog 2.3.2 in the NIR/optical; and high-energy (*CGRO* EGRET, *Fermi* LAT, *INTEGRAL*) catalogs, using the HEASARC

Browse⁷ and DS9⁸ Catalog Search tools. We also examined a list of HESS TeV sources, compiled from several online resources⁹ and publications.

To identify optical/NIR counterparts, we use the X-ray source positional uncertainty, calculated as $\sigma_{\text{pos}} = (\sigma_c^2 + \sigma_{\text{sys}}^2)^{1/2}$, where σ_c is the centroiding (statistical) uncertainty for each individual X-ray source, and σ_{sys} is the systematic pointing uncertainty of *XMM-Newton*¹⁰. In G23.5+0.1 and G25.5+0.0 observations, the σ_c is between 0''.26 and 2''.3 for all the reliably detected sources. The systematic uncertainty σ_{sys} is taken to be 1'', similar to the 2XMM catalog¹¹. We find σ_{pos} to be between 1''.0 and 2''.0 for the sources in G23.5+0.1, and between 1''.1 and 2''.5 for the G25.5+0.0 sources. We consider optical/NIR sources within $3\sigma_{\text{pos}}$ from the X-ray source as possible counterparts. The probability of the association depends on the offset r between the X-ray source and its NIR/optical counterpart. It can be estimated as the probability of finding zero field sources in the circle of radius r , $P = \exp(-\rho\pi r^2)$, where ρ is the average surface density of the optical/NIR sources in the field. We measured $\rho_{\text{USNO-B1}} = 0.007$, $\rho_{2\text{MASS}} = 0.015 \text{ arcsec}^{-2}$ in the G23.5+0.1 field, and $\rho_{\text{USNO-B1}} = 0.006$, $\rho_{2\text{MASS}} = 0.011 \text{ arcsec}^{-2}$ in the G25.5+0.0 field. The offsets and the corresponding probabilities are given in Tables 6 and 7.

4.1. G23.5+0.1

4.1.1. High Energy Counterparts

HESS J1834–087, is located in the vicinity of G23.5+0.1 but just outside the FOV of our *XMM-Newton* observations. However, most of the extended TeV emission from HESS J1834–087 appears to be confined within the radio shell of SNR W41 (see Figure 5). Furthermore, a candidate PWN, possibly associated with W41 and HESS J1834–087, was recently reported by Misanovic et al. (2011). On the other hand, the asymmetry of the HESS source (see Figure 20 in Aharonian et al. 2006) suggests that there may be a fainter TeV source associated with G23.5+0.1. More sensitive TeV observations are needed to confirm this hypothesis. In addition, *Suzaku* has observed a compact TeV source HESS J1832–084, which is apparently

⁷See <http://heasarc.gsfc.nasa.gov/cgi-bin/W3Browse/w3browse.pl>

⁸See <http://hea-www.harvard.edu/RD/ds9/>

⁹E.g., <http://tevcat.uchicago.edu/>; <http://www.mpi-hd.mpg.de/hfm/HESS/pages/home/sources/>.

¹⁰The same method is used in the *XMM-Newton* Serendipitous Source Catalog, Second Version (2XMM), see http://xmmssc-www.star.le.ac.uk/Catalogue/xcat_public_2XMM.html.

¹¹See <http://heasarc.gsfc.nasa.gov/W3Browse/xmm-newton/xmmssc.html>.

coincident with PSR B1829–08 in the G23.5+0.1 field, on April 8, 2011 for 40.3 ks (PI G. Pühlhofer). However, no other information on this new VHE source have been published so far.

We have also searched the *Fermi* LAT 1FGL catalog (Abdo et al. 2010) but found no GeV source within the field of view of our XMM-Newton observation. The nearby 1FGL J1834.3–0842c is located just outside the EPIC FOV and coincides with W41 rather than with G23.5+0.1 (see Figure 5).

4.1.2. Optical and Near-Infrared Counterparts

We found optical/NIR counterparts to all point-like X-ray sources but Sources 3 and 6. We did not find a counterpart to the extended Source 8 (see Table 6). We, however, found that the point source CXOU J183340.3–082830 (see §3.1.1), located within Source 8, has a NIR counterpart 2MASS 18334038–0828304 ($J = 15.7$, $H = 14.0$, $K = 13.5$). More detailed information including magnitudes is provided in Table 6.

4.1.3. Infrared and Radio Counterparts

Only Source 6 and the diffuse Source 8 have no IR counterparts in the *Spitzer*’s GLIMPSE source catalog¹² (see Table 6 for details). We did not find any radio sources coincident with the X-ray point sources. However, the MAGPIS image reveals complex diffuse emission some of which is in the vicinity of B1830–08 and may be related to its PWN or the host SNR. A search in the ATNF pulsar catalog (Manchester et al. 2005) reveals PSR B1830–08, located within the extended *XMM-Newton* Source 8 (in the G23.5+0.1 field) and offset by $\sim 1'$ from its center, and PSR B1829–08 (near the western boundary of the EPIC FOV; see Fig. 1), which does not have an X-ray counterpart. We also notice in the MAGPIS 20 cm image the region of Source 8 appears to be inside a cavity in a large-scale diffuse radio emission (Fig. 1, middle panel) while PSR B1829–08 appears to be surrounded by diffuse radio emission which could be due to a PWN.

¹²Available at <http://irsa.ipac.caltech.edu/data/SPITZER/GLIMPSE/>

4.2. G25.5+0.0

4.2.1. High Energy Counterparts

Figure 1 shows that Source 1 is located within the 1σ extent of HESS J1837–069. From the analysis of the *Chandra* ACIS data GH08 have concluded that AX J1838.0–065 (Source 1) was the likely source of the TeV emission, but suggested that AX J1838.3–062 (Source 15) can also contribute to the TeV emission. The only other X-ray source that might contribute to the TeV emission is Source 9 located within the extent of HESS J1837–069. This source appears to be point-like in X-rays (both in the *Chandra* and *XMM-Newton* images), but it has an interesting extended radio counterpart (see §4.3).

The only other GeV source that falls within the FOV of our observations is 1FGL J1837.5–0659c located in the vicinity of Sources 1, 9, and 15 in the G25.5+0.0 field. Within its positional uncertainty (shown in Figure 2 at 95% confidence), the 1FGL source does not coincide with any of these three X-ray sources (see Figure 2, middle panel). However, the positional uncertainty of this source could be underestimated since this source is marked as confused in the 1FGL catalog¹³. Thus, 1FGL J1837.5–0659c still could be a counterpart to Sources 1, 9 or 15, or it may also simply be a spurious source. As the LAT statistics improves, a better positional accuracy and a search for pulsed signal can allow one to reveal the nature of the GeV source and identify its X-ray counterpart.

AX J1838.0–065 (PSR J1838–0655; Source 1 in the G25.5+0.0 field) is the only *INTEGRAL* source within the FOV of our *XMM-Newton* observations, with the soft-band flux of $(1.4 \pm 0.1) \times 10^{-10}$ erg s^{−1} cm^{−2} (in 20–40 keV) and the hard-band flux of $(2.5 \pm 0.2) \times 10^{-10}$ erg s^{−1} cm^{−2} (in 40–100 keV), according to Bird et al. (2010).

4.2.2. Optical and Near-Infrared Counterparts

We found that about 50% of X-ray sources lack optical and NIR counterparts (sources 1, 3, 9, 13, 15, 16*, 17, 18, 19, 20, and 22 in Table 7). Only two sources lacking optical counterparts appear to have NIR counterparts (sources 11 and 21). More detailed information including magnitudes is provided in Table 7.

¹³Sources labeled “c” (confused) at the end of the 1FGL names are found in regions with bright and/or possibly incorrectly modeled diffuse emission (see http://fermi.gsfc.nasa.gov/ssc/data/access/lat/1yr_catalog/).

4.2.3. Infrared and Radio Counterparts

Most of the sources in this field have counterparts in the GLIMPSE catalog, except for sources 1, 9, 15 and 19 (see Table 7 for details). We also found radio counterparts to several X-ray sources.

In the MAGPIS catalog we found a radio counterpart (G25.31987–0.09825; Helfand et al. 2006) to Source 4 (see Fig. 2), with the offset of just $1''$ from the X-ray position which is much smaller than the restoring beam size¹⁴ of $6''.2 \times 5''.4$. The radio source has the peak 20 cm flux density of 41.10 ± 0.34 mJy.

Source 8* in the G25.5+0.0 field (see Fig. 2) was also found to have a possible radio counterpart, G25.340–0.048, with a flux of 6.7 mJy at $\lambda = 6$ cm (White et al. 2005). However, this radio source is offset from the X-ray source by $3''.5$, while the typical 1σ uncertainty of the radio position is about $1''$ (White et al. 2005).

Third source (in the G25.5+0.0 field) that has a radio counterpart is the star-forming region W42 (Source 6), with integrated flux densities of 1.75 Jy at 20 cm and 1.46 Jy at 6 cm. Source 6 also has multiple counterparts in the Catalog of Star-Forming Regions in the Galaxy (Avedisova 2002). The color-coded color image of G25.5+0.0 (see Figure 2, bottom) reveals a good spatial correlation between Source 6 and the regions of diffuse radio and infrared emission. Finally, the extended X-ray emission near the western boundary of the G25.5+0.0 image (see Section 3.2) has a diffuse radio counterpart which appears to be inside the partial-shell-shaped X-ray emission. We name this diffuse source G25.25+0.28. We also note that Source 21, although lacks a compact radio counterpart, is embedded into a region of faint diffuse emission apparently associated with another star-forming region, which is also the HII region G025.4+00.0 (Paladini et al. 2003), harboring two young stellar objects (YSOs; Urquhart et al. 2009; the nearest of the YSOs is still $20''$ off the Source 21 position).

There are also two bright radio sources in the G25.5+0.0 field (A and B; indicated by arrows in Figure 2, bottom panel) located in the vicinity of HESS J1837–069. As Source 9 is found to be approximately in the middle of the bright linearly extended radio Source B (integrated flux is 7 Jy at 20 cm; Helfand et al. 2006), they are very likely associated (see Fig. 2, bottom panel). Radio source B also has very interesting morphology, with a double nucleus in the middle and two extended arms (jets?) on both sides of the double nucleus (see Fig. 6). The southern arm/jet appears to be better collimated, and it terminates at a

¹⁴We quote only the beam size here since Helfand et al. (2006) do not provide positional uncertainties for the sources; however, we would expect them to be similar to those in White et al. (2005), i.e., typically about $1''$.

bright spot. The ratio of the 6 to 20 cm fluxes suggests a non-thermal spectrum ($\alpha = 0.5 - 1$, $F_\nu \propto \nu^{-\alpha}$) both for extended emission and for each of the nuclei. This radio source does not have any counterparts in *Spitzer* IRAC or 2MASS images. We have also examined the high-resolution *Chandra* ACIS image and found an X-ray counterpart (CXOU J183751.62–064355.4; 273 counts in 20 ks in 0.5–8 keV) coincident with the southern nucleus. The ACIS spectrum fits well an absorbed PL model with $N_H = (1.2 \pm 0.3) \times 10^{23} \text{ cm}^{-2}$, $\Gamma \simeq 1.3_{-0.3}^{+0.4}$, and 0.5–8 keV unabsorbed flux of $1.1 \times 10^{-12} \text{ erg s}^{-1} \text{ cm}^{-2}$ (observed flux is $4.3 \times 10^{-13} \text{ erg s}^{-1} \text{ cm}^{-2}$ in 2–8 keV). The X-ray flux is crudely consistent with the extrapolation of the corresponding radio nucleus counterpart PL spectrum ($\alpha \simeq 0.7$). The reports of HII regions in the vicinity of the radio nucleus (e.g., Avedisova 2002; Giveon et al. 2005) likely stem from the assumed association between the radio source B and a nearby bright IR source detected by the *MSX* satellite. However, higher resolution *Spitzer* IRAC images show that the IR source is $11''$ northwest of the radio nucleus and hence it is not associated with the radio source B. The strong absorption and the lack of an optical counterpart suggest that the source is either extragalactic (hence its light has to penetrate the entire Galactic disk) or it is galactic but intrinsically absorbed (e.g., an HMXB).

5. Source Classification

Based on the measured X-ray properties and multiwavelength properties extracted from catalogs, we attempted to classify the detected sources. In some cases the classifications listed in Tables 6 and 7 are only tentative, based on the limited information available.

The hardness ratio vs. flux (or count rate) plots (analogous to the “color-magnitude diagram” in the optical) are often used for classification of X-ray sources (e.g. Ebisawa et al. 2005; Jonker et al. 2011). In such diagrams the coronally active non-degenerate stars typically occupy the low-HR, low-flux corner and hence are easy to spot. Figure 7 shows such a diagram for our sample.

Another commonly used classification criterion is the X-ray-to-optical flux ratio. Following Maccacaro et al. (1988), we compute $\log(f_X/f_V) = \log f_X + (m_V/2.5) + 5.37$, where m_V is the apparent magnitude in the *V* band. Galaxies, stars, AGNs and X-ray binaries, each fall into a particular range of values of $\log(f_X/f_V)$ (see our Fig. 8 and Fig. 1 in Maccacaro et al. 1988). We estimate the X-ray-to-optical flux ratios for our sources (see Tables 6 and 7 and text below), and use them for source classification, together with other available information.

The X-ray hardness ratio, which is also used for source classification, does not describe

uniquely the X-ray spectrum of a source even in a simple case when the spectrum fits an absorbed PL model (e.g., one often cannot discriminate between a soft, strongly absorbed source and a hard, weakly absorbed source). However, since the statistics precludes spectral fitting for faint sources, the hardness ratio still can be used to differentiate between the most common types of sources: soft, weakly absorbed foreground stars and hard, the strongly absorbed AGNs, seen through the Galactic disk, or cataclysmic variables (CVs) and X-ray binaries (XRBs) in the Galactic bulge. Adding in the flux and IR/NIR/optical fluxes helps to brake the degeneracy because most of strongly absorbed (apparently “hard”) sources with low X-ray fluxes and optical/NIR/IR identifications would be CVs and RS CVns (see, e.g., Figure 3 of Jonker et al. 2011) or embedded coronally active stars (see, e.g., Getman et al. 2011 and references therein).

We also used colors of the optical, NIR and IR counterparts for source classification. Since the optical colors alone are not very informative because of the unknown extinction varying among the sources, we prefer to use NIR and NIR-IR colors which could be used to distinguish between the pre-main and main sequence stars and/or AGNs.

Based on the optical, NIR, and IR data, as well as the flux ratios and X-ray hardness ratios (see Figs. 8 and 9), we find that the majority of the X-ray sources detected in the two SNR fields are foreground main-sequence stars or pre-main sequence stars associated with star-forming regions or AGNs. Several objects are likely to be background CVs or quiescent XRBs, although we cannot completely rule out the possibility that some of the faint X-ray sources with no optical or infrared counterparts may be isolated neutron stars and pulsars. The current population models for different classes of X-ray sources are fairly uncertain (see e.g., Ebisawa et al. 2005; Motch et al. 2010 and references therein) and provide only spatially averaged estimates, while the actual distribution of different types of objects can be quite inhomogeneous throughout the Galactic plane even on a degree angular scales. Nevertheless we used the estimates provided in Table 7 of Motch et al. (2010) for the *XMM-Newton* Galactic Plane Survey (XGPS) covering 3 square degree region of the plane between $l = 19^\circ$ and 22° (i.e. nearly adjacent to our fields). Scaling down the XGPS estimates by area, we would expect to detect 5-9 AGNs, 4 coronally active stars, and about 2 accreting binaries down to the flux level of 5×10^{-14} erg s $^{-1}$ cm $^{-2}$. The total number of sources we detected above this flux level is 70% larger suggesting some unaccounted population or reflecting the uncertainties of the population estimates. One possible reason is the starforming activity associated the G25.5+0.0 filed (see below) likely resulting in a larger number of young magnetically active stars which we detect in X-rays. Part of the excess among the hard sources is due to the two young pulsars but there still remain 2-3 unaccounted sources which could be NSs (see Tables 6 and 7).

Among the detected and classified sources particularly interesting are the following.

- Source 1 (PSR J1838–0655), in the G25.5+0.0 field, is a young pulsar whose pulsations have been found with *RXTE* (GH08).
- We confirm the previously suggested (GH08) interpretation of AX J1837.3–0652 (Source 15) as a PWN based on the extended X-ray emission and a lack of a NIR/IR counterpart.
- Source 9 (having an extended radio counterpart) in the same field could be a peculiar radio galaxy seen through the Galactic disk or an HMXB in the low state.
- A partial shell diffuse source G25.25+0.28, resolved in X-rays and radio, is likely to be an uncataloged SNR.
- In the same field we also detected several X-ray sources apparently associated with a massive young cluster W42 (based on the location and correlations with IR sources).
- In the G23.5+0.1 field we discovered an extended Source 8 which is likely an X-ray PWN powered by PSR B1830–08.

6. Discussion and Summary

6.1. The field of G23.5+0.1

In the G23.5+0.1 field we found an extended ($\sim 4'$ in diameter) X-ray emission surrounding PSR B1830–08, which is likely a PWN. Its X-ray efficiency in 0.5–8 keV, $\eta_{0.5-8} \equiv L_{0.5-8}/\dot{E} = 5 \times 10^{-3}$, is well within the range measured for other PWNe (Kargaltsev & Pavlov 2008). The undetected pulsar must be at least a factor of 10 less luminous than the PWN, which is not unusual. The extended X-ray emission has a rather amorphous shape which does not appear as a bow-shock PWN (see also Esposito et al. 2011). This suggests that despite the apparently high but rather uncertain transverse velocity of 751 ± 163 km s $^{-1}$ (calculated for the dispersion measure distance of 4.7 kpc; see Hobbs et al. 2005), PSR B1830–08 either does not move supersonically (because the distance is strongly overestimated) or the detected extended X-ray emission does not come from the PWN (in which case it might be associated with an SNR). The faint diffuse radio emission north of PSR B1830–08 (see Fig. 1, bottom and Figure 5) could be related to the host SNR. The thermal X-ray emission from the SNR shell could be strongly absorbed due to the large N_H . If this radio emission is indeed due to the host SNR of PSR B1830–08, then the pulsar must be

much younger than its spin-down age of 147 kyrs. This is possible, and indeed a similar age discrepancy was found, e.g., for PSR J0538+2817 in SNR S147 (Ng et al. 2007). Alternatively, it is possible that the diffuse radio emission comes from the relic PWN of PSR B1830–08, where the electrons are too “cold” to emit X-rays via synchrotron mechanism. A number of relic PWNe has been recently found (see Kargaltsev & Pavlov 2010 for a review), mainly in the TeV observations. It is possible that a deeper TeV exposure would detect a relic PWN of PSR B1830–08, a hint of which might be already seen (§4.1). If the radio emission north of PSR B1830–08 is due to its relic PWN, the host radio SNR shell may have either become too dim or too large to be seen in the X-ray and radio images. Additional confusion is caused by the highly nonuniform, complex radio background due to the adjacent W41 southeast of G23.5+0.1 and the radio-bright (apparently star-forming) region northeast of the pulsar (which correlates with IR emission and has a thermal spectrum in the radio; Shaver & Goss 1970).

We also detected seven other point sources in the field of G23.5+0.1. All but one (Source 6) were found to have IR counterparts and hence are likely foreground stars, CVs, XRBs, or AGNs seen through the Galactic disk (see Table 6). Source 6 has too few X-ray counts to make a conclusion about its nature, it could be an AGN or a faint pulsar. Finally, there are two possible high-energy sources which we do not detect in our observation. One is PSR B1829–08, which has a spin-down age similar to that of PSR B1830–08 and located at nearly the same distance (according to the Galactic electron density model by Taylor & Cordes 1993) but has the spin-down power a factor of 62 lower than B1830–08. However, the surrounding diffuse radio emission and the good spatial coincidence with the TeV source HESS J1832–084 may indicate the presence of a relic PWN whose electrons are too cold to emit X-rays via the synchrotron mechanism. We also have not detected SGR 1833–0832 in our *XMM-Newton* observation. Assuming a plausible spectral model for the quiescent SGR spectrum and $N_H = 3 \times 10^{22} \text{ cm}^{-2}$, we find that its quiescent absorbed flux is at least a factor of 10^3 lower than its active state flux. This places a very low limit on the quiescent SGR luminosity, $L \lesssim 10^{32} (d/8 \text{ kpc})^2 \text{ erg s}^{-1}$ (in 1–10 keV, unabsorbed, assuming $N_H = 3 \times 10^{22} \text{ cm}^{-2}$), a factor of 4,000 smaller than that of SGR 0526–66 measured 30 years after the giant flare (Tiengo et al. 2009). This suggests that SGRs can maintain an elevated luminosity decades after the period of activity, well above the “truly quiescent” level. One of the implications is that there may be a significant number of quiescent SGRs, which we have not detected in X-rays so far.

6.2. The field of G25.0+0.0

The only large-scale diffuse emission we found in the G25.0+0.0 field is a shell-like source G25.25+0.28. However, its low surface brightness in X-rays precludes any spectral analysis. G25.25+0.28 is too far from the center of G25.0+0.0 to contribute to the G25.0+0.0 emission seen in the *ASCA* images. We conclude that the previous claims of extended emission and the reports of the X-ray SNR candidate G25.5+0.0 (e.g., Bamba et al. 2003) were likely the result of overlapping *ASCA* PSF wings from several adjacent unresolved sources. One of these, Source 6, has a thermal-like X-ray spectrum and positionally coincides with the core of the young, obscured star-forming region W42. Although Source 6 appears to be point-like at the *XMM-Newton* resolution, it is resolved into three sources in the *Chandra* ACIS image.

XMM-Newton and *Chandra* also resolved two *ASCA* sources, one of which (AX J1838.0–0655) is a recently discovered young pulsar (J1838–0655) while the other one (AX J1837.3–0652) is likely a PWN powered by a yet undetected pulsar (GH08). Although each of these two objects could be accompanied by an SNR, the radio shell could have dissipated significantly (the pulsar’s spin-down age is 23 kyrs) while the thermal X-ray emission must be severely attenuated by the large absorbing column.

We also identified a peculiar radio counterpart to the Source 9 which could be a heavily obscured radio galaxy with powerful jets (cf. M87 or Centaurus A) and double nucleus (but not a blazar since the jets are at significant angle with respect to the observer). Similar sources (e.g., 4C 65.15 and 3C433) have been described by Miller & Brandt (2009) and classified as FR II radio galaxies with asymmetric environments. Alternatively, Source 9 could be a heavily absorbed microquasar (e.g., similar to 1E 1740.7–2942) but in the very low state. Note that a similar double-lobed radio and X-ray source was recently found within TeV J2032+4130 (Butt et al. 2008). All the three sources could contribute to the TeV emission from HESS J1837–069 and the possible GeV emission from the *Fermi* source 1FGL J1837.5–0659c.

The only other sources that do not have IR, NIR, or optical counterparts are Sources 13 and 19. Particularly interesting is Source 19 that has $HR \simeq -0.04$, suggesting a soft and relatively weakly absorbed X-ray spectrum that could belong to a foreground star, but the lack of any optical/NIR counterpart disfavors such a scenario. AGNs, quiescent XRBs, and CVs are expected to have much harder spectra. A plausible remaining option is a nearby, “X-ray dim” isolated neutron star (see, e.g., Kaplan 2008 for a review). However, the scarce data available make difficult any firm conclusions. Deeper optical/NIR observations are needed to make a firm conclusion on the nature of this source.

We would like to thank Richard White for the help with MAGPIS images, Aya Bamba for providing references on ASCA observations, and Neil Brandt for the discussion of Source 9 in the G25.0+0.0 field. We also thank Konstantin Getman for useful discussion about the properties of young stars. We are grateful to the anonymous referee for very careful reading and useful suggestions. The work on this project was partly supported through the NASA grants NNX06AG36G, NNX09AC81G and NNX09AC84G, and National Science Foundation grants No. 0908733 and 0908611. The work by G. G. P. was partly supported by the Ministry of Education and Science of the Russian Federation (contract 11.634.31.0001).

REFERENCES:

- Abdo, A. A., Ackermann, M., Ajello, M., et al. 2009, *ApJS*, 183, 46
- Abdo, A. A., Ackermann, M., Ajello, M., et al. 2010, *ApJS*, 188, 405
- Aharonian, F., Akhperjanian, A. G., Bazer-Bachi, A. R., et al. 2006, *ApJ*, 636, 777
- Avedisova, V. S. 2002, *Astronomy Reports*, 46, 193
- Bamba, A., Ueno, M., Koyama, K., & Yamauchi, S. 2003, *ApJ*, 589, 253
- Bernardini, F., Israel, G. L., Dall’Osso, S., et al. 2009, *A&A*, 498, 195
- Bird, A. J., Bazzano, A., Bassani, L., et al. 2010, *ApJS*, 186, 1
- Blum, R. D., Conti, P. S., & Damini, A. 2000, *AJ*, 119, 1860
- Butt, Y. M., Combi, J. A., Drake, J., Finley, J. P., Konopelko, A., Lister, M., Rodriguez, J., & Shepherd, D. 2008, *MNRAS*, 385, 1764
- Clifton, T. R., & Lyne, A. G. 1986, *Nature*, 320, 43
- Condon, J. J., Cotton, W. D., Greisen, E. W., Yin, Q. F., Perley, R. A., Taylor, G. B., & Broderick, J. J. 1998, *AJ*, 115, 1693
- Ebisawa, K., Tsujimoto, M., Paizis, A., et al. 2005, *ApJ*, 635, 214
- Esposito, P., Israel, G. L., Turolla, R., et al. 2011, *MNRAS*, 416, 205
- Gaensler, B. M., & Johnston, S. 1995, *MNRAS*, 275, L73
- Giveon, U., Becker, R. H., Helfand, D. J., & White, R. L. 2005, *AJ*, 130, 156
- Göğüş, E., Cusumano, G., Levan, A. J., et al. 2010, *ApJ*, 718, 331
- Gelbord, J. M., Barthelmy, S. D., Baumgartner, W. H., et al. 2010, *GRB Coordinates Network, Circular Service*, 10526, 1 (2010), 526, 1
- Getman, K. V., Broos, P. S., Feigelson, E. D., et al. 2011, *ApJS*, 194, 3
- Gotthelf, E. V., & Halpern, J. P. 2008, *ApJ*, 681, 515 (GH08)
- Green, D. A. 2009, *Bulletin of the Astronomical Society of India*, 37, 45 (available on the World-Wide-Web at "<http://www.mrao.cam.ac.uk/surveys/snrs/>")
- Helfand, D. J., Becker, R. H., White, R. L., Fallon, A., & Tuttle, S. 2006, *AJ*, 131, 2525
- Hobbs, G., Lyne, A. G., Kramer, M., Martin, C. E., & Jordan, C. 2004, *MNRAS*, 353, 1311

- Hobbs, G., Lorimer, D. R., Lyne, A. G., & Kramer, M. 2005, *MNRAS*, 360, 974
- Jonker, P. G., Bassa, C. G., Nelemans, G., et al. 2011, *ApJS*, 194, 18
- Kaplan, D. L. 2008, 40 Years of Pulsars: Millisecond Pulsars, Magnetars and More, AIP Conf. Proc., 983, 331
- Kargaltsev, O., & Pavlov, G. G. 2008, in 40 Years of Pulsars: Millisecond Pulsars, Magnetars, and More, eds. C. Bassa, A. Cumming, V. M. Kaspi, & Z. Wang, AIP Conf. Proc., 983, 171
- Kargaltsev, O., & Pavlov, G. 2010, in X-ray Astronomy 2009: Present Status, Multi-Wavelength Approach And Future Perspectives, eds. A. Comastri, M. Cappi, & L. Angelini, AIP Conf. Proc., 1248, 25
- Kaspi, V. M. 2007, *Ap&SS*, 308, 1
- De Luca, A., Caraveo, P. A., Mereghetti, S., Negroni, M., & Bignami, G. F. 2005, *ApJ*, 623, 1051
- Maccacaro, T., Gioia, I. M., Wolter, A., Zamorani, G., & Stocke, J. T. 1988, *ApJ*, 326, 680
- Manchester, R. N., Hobbs, G. B., Teoh, A., & Hobbs, M. 2005, *AJ*, 129, 1993
- Miller, B. P., & Brandt, W. N. 2009, *ApJ*, 695, 755
- Misanovic, Z., Kargaltsev, O., & Pavlov, G. G. 2010, *ApJ*, 725, 931
- Misanovic, Z., Kargaltsev, O., & Pavlov, G. G. 2011, *ApJ*, 735, 33
- Monet, D. G., Levine, S. E., Canzian, B., et al. 2003, *AJ*, 125, 984
- Motch, C., Warwick, R., Cropper, M. S., et al. 2010, *A&A*, 523, A92
- Ng, C.-Y., Romani, R. W., Briskin, W. F., Chatterjee, S., & Kramer, M. 2007, *ApJ*, 654, 487
- Paladini, R., Burigana, C., Davies, R. D., Maino, D., Bersanelli, M., Cappellini, B., Platania, P., & Smoot, G. 2003, *A&A*, 397, 213
- Pavlov, G. G., Kargaltsev, O., Wong, J. P., & Garmire, G. P. 2009, *ApJ*, 691, 458
- Seward, F., Slane, P., Randall, S., et al. 2010, Chandra Supernova Remnant Catalog, Harvard-Smitonian Center for Astrophysics, Harvard University, USA (available on the World-Wide-Web at "<http://hea-www.harvard.edu/ChandraSNR/>").
- Shaver, P. A., & Goss, W. M. 1970, *Australian Journal of Physics Astrophysical Supplement*, 14, 133

- Skrutskie, M. F., Cutri, R. M., Stiening, R., et al. 2006, *AJ*, 131, 1163
- Taylor, J. H., & Cordes, J. M. 1993, *ApJ*, 411, 674
- Tiengo, A., Esposito, P., Mereghetti, S., et al. 2009, *MNRAS*, 399, L74
- White, R. L., Becker, R. H., & Helfand, D. J. 2005, *AJ*, 130, 586
- Ueno, M. 2005, Ph.D. Thesis, Kyoto University
- Urquhart, J. S., Hoare, M. G., Purcell, C. R., et al. 2009, *A&A*, 501, 539

Table 1: Observation log

Field	Obs ID	Date	Pointing coordinates R.A. and Dec. (J2000)		Exposure PN ^a ks	Exposure MOS1 ^a ks	Exposure MOS2 ^a ks
G23.5+0.1	0400910101	2006-09-16	18:33:33.8	−08:25:30.3	10.54	12.17	12.18
G25.5+0.0	0400910301	2006-10-18	18:37:10.0	−06:39:49.7	7.53	9.17	9.17
G25.5+0.0	0400910401	2006-10-18	18:37:43.2	−06:43:38.0	7.53	9.17	9.17

^aScientific exposures used in the analysis.

Table 2: X-ray sources in the G23.5+0.1 field

Source ID ^a	Flux ^b 10 ^{−14} c.g.s.	C _{PN} ^c counts/ks	C _{MOS1} ^c counts/ks	C _{MOS2} ^c counts/ks	S/N	HR	R.A. deg	Dec. deg	σ _{pos} ^d arcsec
1	21.9±0.7	72.4±2.9	19.3±1.3	18.1±1.4	31.4	−0.83 ± 0.08	278.438633	−8.307803	1.03
2	24.8±2.3	10.1±1.3	4.9±0.8	4.0±0.7	11.3	1.0 _{−0.10}	278.324492	−8.420513	1.20
3	44.0±6.4	4.1±1.3 ^e	3.9±0.7	3.6±0.6	7.3	1.0 _{−0.12}	278.498733	−8.373778	1.46
4	4.0±0.8	5.0±1.4 ^e	4.3±0.8	3.0±0.5	7.3	−0.19 ± 0.57	278.279851	−8.252994	1.06
5	9.2±1.8	3.3±1.1 ^e	2.8±0.5	2.3±0.4	6.5	1.0 _{−0.18}	278.344773	−8.402801	1.70
6	7.0±1.1	3.2±1.1	2.4±0.5	2.1±0.4	6.0	1.0 _{−0.26}	278.340301	−8.509183	1.52
7	1.9±0.4	3.0±0.9	...	1.8±0.4	5.0	−0.05 ± 0.75	278.336846	−8.566790	1.96

Note. — Properties of X-ray sources found with the *edetect_chain* automatic detection procedure. The uncertainties correspond to 68% confidence interval. Since HR cannot exceed 1 by definition, we quote only the lower bound (at 68% confidence) in the cases when the formal upper bound is > 1.

^aSource ID number used throughout the paper.

^bObserved flux in 0.2–12 keV in units of 10^{−14} erg s^{−1} cm^{−2}, estimated using ECFs. The uncertainties do not include systematic error which can be significant for strongly absorbed sources (see §3).

^cObserved, background-subtracted EPIC count rate for PN, MOS1, and MOS2 in 0.2–12 keV.

^dPosition uncertainty (see §4.2).

^eIn PN, the source partly falls within the chip gap which reduces the count rate.

Table 3: X-ray sources in the G25.5+0.0 field

Source ID ^a	Flux ^b 10 ⁻¹⁴ c.g.s.	C _{PN} ^c counts/ks	C _{MOS1} ^c counts/ks	C _{MOS2} ^c counts/ks	S/N	HR	R.A. deg	Dec. deg	σ_{pos} ^d arcsec
1	951±41	70.0±3.8	18.4	1.0 _{-0.06}	279.513756	-6.925462	1.07
2	11.5±0.8	24.3±1.3	10.4±1.1	9.0±1.0	21.6	-0.70 ± 0.15	279.495002	-6.805702	1.12
3	79.5±6.7	17.6±1.6	...	6.5±0.9	13.1	1.0 _{-0.08}	279.499546	-6.822605	1.18
4*	30.6±2.8	7.5±0.8	2.7±0.4	2.9±0.5	12.7	1.0 _{-0.13}	279.460173	-6.815297	1.21
5*	9.9±0.6	9.2±0.9	5.7±0.9	3.9±0.5	14.2	0.52 ± 0.30	279.262722	-6.823484	1.24
6	90.8±5.4	30.4±2.1	8.6±1.0	9.8±1.1	19.0	0.86 ± 0.12	279.563358	-6.799838	1.30
7*	8.2±0.4	22.9±1.2	8.1±1.0	4.6±0.5	20.6	-0.87 ± 0.10	279.298147	-6.554131	1.32
8*	20.7±2.0	5.8±0.7	1.0±0.3	2.1±0.4	9.9	1.0 _{-0.10}	279.424316	-6.775722	1.32
9	46.9±5.9	7.2±1.1	...	3.6±0.7	13.1	1.0 _{-0.13}	279.464660	-6.895446	1.36
10*	4.3±0.5	5.8±0.7	1.2±0.3	1.8±0.4	9.8	0.67 ± 0.32	279.404399	-6.735200	1.45
11	37.8±4.3	5.9±1.0	2.0±0.4	1.5±0.4	7.9	1.0 _{-0.11}	279.500926	-6.622271	1.55
12*	1.6±0.2	5.8±0.7	1.3±0.4	1.4±0.4	9.5	-0.36 ± 33	279.388669	-6.667137	1.59
13	23.8±4.1	3.7±0.9	1.5±0.5	1.5±0.5	5.8	1.0 _{-0.51}	279.579818	-6.729061	1.61
14	4.5±0.7	5.5±0.7	1.3±0.5	1.0±0.3	8.3	0.69 ± 0.30	279.282215	-6.858810	1.74
15	115±15	17.3±1.6	7.0±0.9	5.5±0.6	15.1	1.0 _{-0.13}	279.339761	-6.874498	2.51
16*	21.5±2.7	4.6±0.7	2.3±0.4	2.3±0.4	10.2	1.0 _{-0.14}	279.371524	-6.614574	1.87
17	8.4±1.7	6.1±1.0	2.1±0.4	1.4±0.4	8.2	0.87 ± 0.20	279.451552	-6.653508	1.63
18	6.5±1.0	6.0±1.0	2.4±0.6	1.4±0.5	7.5	0.67 ± 0.31	279.202677	-6.540072	1.66
19	2.4±0.4	2.6±0.6	1.5±0.4	1.4±0.4	7.1	-0.04 ± 0.37	279.336448	-6.538502	1.74
20	9.9±2.1	2.8±0.8	0.9±0.4	1.4±0.5	4.8	1.0 _{-0.26}	279.145257	-6.728290	1.90
21	6.2±1.2	4.0±0.6	1.0±0.3	1.1±0.3	7.7	1.0 _{-0.36}	279.393015	-6.683063	1.76
22	1.0±0.2	3.5±0.6	1.1±0.3	0.9±0.3	7.1	-0.14 ± 0.73	279.359209	-6.704057	1.67
23	1.4±0.3	2.9±0.8	1.0±0.3	0.7±0.3	5.0	0.24 ± 0.71	279.232527	-6.710708	1.73

Note. — Properties of X-ray sources from the *edetect_chain* automatic detection procedure. Asterisks denote the sources detected in both observations of the G25.5+0.0 field. The uncertainties correspond to 68% confidence interval. Since HR cannot exceed 1 by definition, we quote only the lower bound (at 68% confidence) in the cases when the formal upper bound is > 1 .

^aSource ID number used throughout the paper.

^bObserved flux in 0.2–12 keV in units of 10⁻¹⁴ erg s⁻¹ cm⁻², estimated using ECFs. The uncertainties do not include systematic error which can be significant for strongly absorbed sources (see §3).

^cObserved, background-subtracted EPIC count rates for PN, MOS1, and MOS2 in 0.2–12 keV (averaged if the source is detected in both fields).

^dPosition uncertainty (see §4.2).

Table 4: Absorbed *mekal* model fits to the spectra of sufficiently bright sources

Field (Source ID)	N_H 10^{21} cm^{-2}	kT keV	Abundance ^a % Solar	Normalization ^b	Flux ^c $10^{-13} \text{ erg cm}^{-2} \text{ s}^{-1}$	χ^2_ν /d.o.f.
G23.5+0.1 (Source 1)	1.3 ± 0.2	0.59 ± 0.24	10	$6.0^{+0.6}_{-0.5} \times 10^{-4}$	3.5 ± 0.3	1.20/71
G25.5+0.0 (Source 6)	28.3 ± 4.2	$2.20^{+0.37}_{-0.26}$	110	$8.4^{+1.8}_{-1.6} \times 10^{-4}$	9.6 ± 1.9	1.05/52
G25.5+0.0 (Source 7)	$3.8^{+1.7}_{-0.5}$	0.28 ± 0.07	330	$7.5^{+3.4}_{-0.7} \times 10^{-4}$	4.6 ± 2.5	0.99/21

Note. — The uncertainties are given at the 68% confidence level for a single interesting parameter.

^aAbundance is the number of metal nuclei per Hydrogen nucleus relative to the solar value. Helium abundance is fixed at the cosmic value (9.77%). (See <http://heasarc.gsfc.nasa.gov/docs/xanadu/xspec/manual/XSmodelMeka.html> for details).

^bNormalization of the *mekal* model defined at <http://heasarc.gsfc.nasa.gov/docs/xanadu/xspec/manual/XSmodelMeka.html>.

^cUnabsorbed fluxes given for the same energy bands as the absorbed fluxes in the text, i.e., 0.3–5 keV, 1–8 keV, and 0.3–2 keV (top to bottom, respectively).

Table 5: Absorbed PL model fits to the spectra of sufficiently bright sources

Field (Source ID)	N_H 10^{22} cm^{-2}	Γ	Normalization ^a	Flux ^b $10^{-13} \text{ erg cm}^{-2} \text{ s}^{-1}$	χ^2_ν /d.o.f.
G23.5+0.1 (Source 8)	3.9 ± 1.9	2.3 ± 0.8	$1.8^{+9.0}_{-1.8} \times 10^{-4}$	5.6 ± 3.0	1.31/48
G25.5+0.0 (Source 1)	$5.2^{+1.0}_{-0.8}$	$1.2^{+0.3}_{-0.1}$	$1.1^{+0.7}_{-0.4} \times 10^{-3}$	124 ± 20	0.70/41
G25.5+0.0 (Source 6)	$2.9^{+0.6}_{-0.5}$	$2.8^{+0.4}_{-0.3}$	$5.8^{+4.1}_{-2.2} \times 10^{-4}$	9.5 ± 1.8	1.31/52
G25.5+0.0 (Source 15)	$6.7^{+3.8}_{-2.2}$	$2.1^{+0.9}_{-0.6}$	$2.8^{+10.5}_{-2.8} \times 10^{-4}$	7.4 ± 2.3	0.95/45

Note. — The uncertainties are given at the 68% confidence level for a single interesting parameter.

^aSpectral flux density at 1 keV, in photons $\text{s}^{-1} \text{ cm}^{-2} \text{ keV}^{-1}$.

^bUnabsorbed fluxes given for the same energy bands as the absorbed fluxes in the text, i.e. 1–10 keV, 1–11 keV, 1–8 keV, and 2–10 keV (top to bottom, respectively).

Table 6. Candidate optical and infrared counterparts and the proposed classification of the X-ray sources in the G23.5+0.1 field.

Source	Offset ^a arcsec	Prob. ^b	J^c	H^c	K^c	Offset ^d arcsec	Prob. ^e	V^f	I^f	$\log(\frac{f_X}{f_V})^g$	Offset ^h arcsec	4.5mag ⁱ	8.0mag ^j	Class ^j
1	1.3 ± 1.1	0.92	8.5 ± 0.03	8.2 ± 0.06	8.0 ± 0.02	1.3 ± 1.1	0.96	10.1	9.2	-3.1	1.4 ± 1.1	8.03 ± 0.04	7.93 ± 0.03	F8-star
2	0.9 ± 1.2	0.96	15.5 ± 0.09	14.2 ± 0.10	13.7 ± 0.08	> 0.1	0.8 ± 1.2	13.25 ± 0.23	...	CV?
3	> 0.1	3.9 ± 1.5	13.34 ± 0.23	...	AGN/CV/NS
4	0.5 ± 1.1	0.99	12.2 ± 0.03	11.4 ± 0.03	11.1 ± 0.03	0.4 ± 1.1	0.99	16.9	14.2	-1.1	0.7 ± 1.1	10.81 ± 0.06	10.77 ± 0.10	M/K-dwarf
5	1.4 ± 1.7	0.91	17.4 ± 0.00	15.1 ± 0.00	13.8 ± 0.09	> -0.3	1.4 ± 1.7	12.76 ± 0.11	...	AGN/PMS-star/CV
6	> -0.2	AGN/CV/NS?
7	1.5 ± 2.9	0.90	7.2 ± 0.02	7.0 ± 0.05	7.0 ± 0.02	1.4 ± 2.0	0.96	8.1	7.6	-5.2	1.3 ± 2.0	6.95 ± 0.05	6.91 ± 0.03	A5-star

Note. — The uncertainties are given at the 68% confidence

^aOffset between the X-ray source and its 2MASS counterpart.

^bProbability of the 2MASS source being a true counterpart to the X-ray source.

^cMagnitudes from the 2MASS All-Sky Catalog of Point Sources (Skrutskie et al. 2006).

^dOffset between the X-ray source and its USNO-B1.0 counterpart

^eProbability of the USNO-B1.0 source being a true counterpart to the X-ray source.

^fMagnitudes from the USNO-B1.0 catalog (Monet et al. (2003)).

^gOptical-to-X-ray flux ratio (see §5).

^hOffset between the X-ray source and its GLIMPSE counterpart.

ⁱMagnitudes from the GLIMPSE catalog (<http://irsa.ipac.caltech.edu/data/SPITZER/GLIMPSE/>).

^jProbable classification of the sources.

Table 7. Candidate optical and infrared counterparts and the proposed classification of the X-ray sources in the G25.5+0.0 field.

Source	Offset ^a arcsec	Prob. ^b	J^c	H^c	K^c	Offset ^d arcsec	Prob. ^e	V^f	I^f	$\log(\frac{f_X}{f_V})^g$	Offset ^h arcsec	4.5mag ⁱ	8.0mag ^j	Class ^j
1	> 1.8	PSR
2	1.1 ± 1.2	0.96	6.9 ± 0.02	6.5 ± 0.02	6.4 ± 0.02	0.8 ± 1.2	0.99	8.4	7.3	$-4.1 \pm 0.5 \pm 1.2$	6.37 ± 0.03	G5-star
3	$> 0.4 \pm 2.9 \pm 1.2$	13.69 ± 0.22	AGN/CV/PMS-star?
4*	3.6 ± 1.2	0.64	15.0 ± 0.06	14.4 ± 0.07	12.7 ± 0.00	3.4 ± 1.2	0.80	18.9	16.8	$> 0.5 \pm 3.2 \pm 1.2$	13.23 ± 0.20	CV?
5*	2.1 ± 1.3	0.86	9.4 ± 0.02	8.4 ± 0.02	8.0 ± 0.02	1.6 ± 1.3	0.96	...	12.0	$> 0.6 \pm 1.4 \pm 1.3$	7.85 ± 0.04	7.72 ± 0.03	...	M-dwarf
6	1.3 ± 1.3	0.95	10.0 ± 0.02	8.7 ± 0.02	7.8 ± 0.02	0.8 ± 1.3	0.99	...	12.9	$> 1.3 \pm 0.0 \pm 1.3$...	$\sim 0.2^a$...	W42 core
7*	2.2 ± 1.3	0.84	8.8 ± 0.02	8.6 ± 0.02	8.5 ± 0.02	2.3 ± 1.3	0.91	9.8	9.1	$-3.6 \pm 1.3 \pm 1.3$	8.53 ± 0.06	8.48 ± 0.04	...	F8-star
8*	0.3 ± 1.3	0.99	15.7 ± 0.08	15.0 ± 0.00	14.6 ± 0.00	0.5 ± 1.3	0.99	...	17.4	$> 0.6 \pm 2.6 \pm 1.3$	13.06 ± 0.20	AGN?
9	> 0.1	AGN/MQSO
10*	1.5 ± 1.5	0.92	12.1 ± 0.04	11.1 ± 0.04	10.6 ± 0.06	1.4 ± 1.5	0.96	17.3	13.3	$-1.4 \pm 2.2 \pm 1.5$	10.51 ± 0.06	11.02 ± 0.15	...	K/M-dwarf
11	2.9 ± 1.6	0.74	15.7 ± 0.10	13.2 ± 0.00	12.2 ± 0.00	$> 0.4 \pm 2.7 \pm 1.6$	12.08 ± 0.12	AGN/CV/PMS-star?
12*	1.5 ± 1.6	0.92	12.3 ± 0.03	11.7 ± 0.02	11.5 ± 0.02	1.3 ± 1.6	0.97	15.6	13.2	$-2.1 \pm 1.3 \pm 1.6$	11.20 ± 0.08	11.15 ± 0.14	...	K-dwarf
13	> -0.2	AGN/CV/NS?
14	1.0 ± 1.8	0.97	13.4 ± 0.03	12.8 ± 0.04	11.6 ± 0.00	1.1 ± 1.8	0.98	16.2	13.7	$-1.7 \pm 3.2 \pm 1.8$	12.30 ± 0.09	M-dwarf
15	> 0.9	PWN
16	$> -0.1 \pm 1.5 \pm 1.9$	12.58 ± 0.12	11.01 ± 0.15	...	AGN/PMS-star
17	$> 0.2 \pm 0.0 \pm 1.7$	12.18 ± 0.11	AGN/PMS-star
18	$> 0.3 \pm 1.4 \pm 1.7$	12.60 ± 0.13	AGN/PMS-star
19	> 0.2	INS?
20	$> -0.3 \pm 1.2 \pm 1.9$	12.64 ± 0.11	AGN/PMS-star
21	2.2 ± 1.8	0.85	13.4 ± 0.04	12.1 ± 0.05	11.3 ± 0.05	$> 0.0 \pm 1.6 \pm 1.8$	10.73 ± 0.15	10.25 ± 0.16	...	K/M-dwarf/PMS-star
22	$> -0.2 \pm 0.7 \pm 1.7$	12.10 ± 0.11	F/G/K/M-dwarf/PMS-star
23	1.7 ± 1.8	0.90	13.8 ± 0.03	12.8 ± 0.04	12.6 ± 0.30	1.4 ± 1.8	0.96	17.6	15.2	$-1.4 \pm 1.9 \pm 1.8$	12.28 ± 0.10	K/M-dwarf

Note. — The uncertainties are given at the 68% confidence

^aOffset between the X-ray source and its 2MASS counterpart.

^bProbability of the 2MASS source being a true counterpart to the X-ray source.

^cMagnitudes from the 2MASS All-Sky Catalog of Point Sources (Skrutskie et al. 2006).

^dOffset between the X-ray source and its USNO-B1.0 counterpart

^eProbability of the USNO-B1.0 source being a true counterpart to the X-ray source.

^fMagnitudes from the USNO-B1.0 catalog (Monet et al. (2003)).

^gOptical-to-X-ray flux ratio (see §5).

^hOffset between the X-ray source and its GLIMPSE counterpart.

ⁱMagnitudes from the GLIMPSE catalog (<http://irsa.ipac.caltech.edu/data/SPITZER/GLIMPSE/>).

^jProbable classification of the sources.

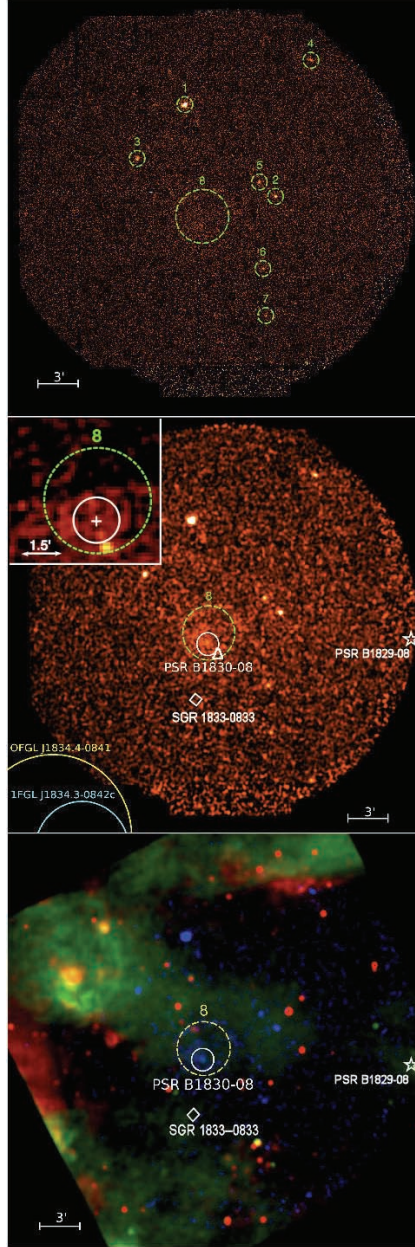


Fig. 1.— *Top*: Combined PN+MOS1+MOS2 image of the G23.5+0.1 field in the 0.2–10 keV band. The small green circles mark point-like (or compact) X-ray sources found by the SAS source detection procedure. The large green circle shows the diffuse Source 8 identified visually (see §3). Source numbering corresponds to that in Table 2. *Middle*: The same image as in the top panel but smoothed with the gaussian (FWHM 6"). The white circle shows the position of PSR B1830-08. Small white triangle shows the position of CXOU J183340.3-082830 found in the *Chandra* image (see text). The inset shows the *Chandra* ACIS image (discussed in §) with the same circles as in the EPIC image and the cross at the radio position of the pulsar. *Bottom*: Multiwavelength image of G23.5+0.1 field (blue: 0.2–10 keV combined EPIC image; green: 20 cm radio image from MAGPIS; red: *Spitzer* IRAC image at 8.0 μm).

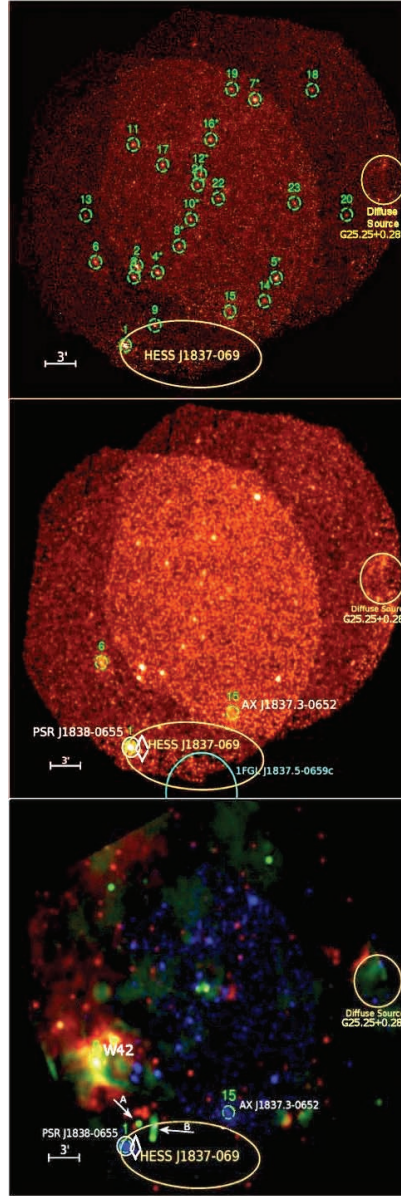


Fig. 2.— *Top*: Combined PN+MOS1+MOS2 image of the G25.5+0.0 field in the 0.2–10 keV band obtained by merging the data from two *XMM-Newton* observations of the field (see Table 1). The small green circles mark point-like X-ray sources found by the automatic source detection procedure. The yellow ellipse near the western edge of the FOV shows a diffuse shell-like emission (G25.25+0.28; see §4.3), which was not detected automatically. The source numbering corresponding to that in Table 3. The yellow elliptical region at the southern edge of the FOV shows the 1σ extent of the TeV emission from HESS J1837–069. *Middle*: The same image as in the top panel but smoothed with the gaussian (FWHM 6''). The white diamond region marks the positions of the *INTEGRAL* source coincident with AX J1838.0–065. The white circle marks PSR J1838–0655 and its PWN coincident with Source 1. *Bottom*: Multiwavelength image of G25.5+0.0 field (blue: 0.2–10 keV combined EPIC image; green: 20 cm radio image from MAGPIS; red: *Spitzer* IRAC image at 8.0 μ m).

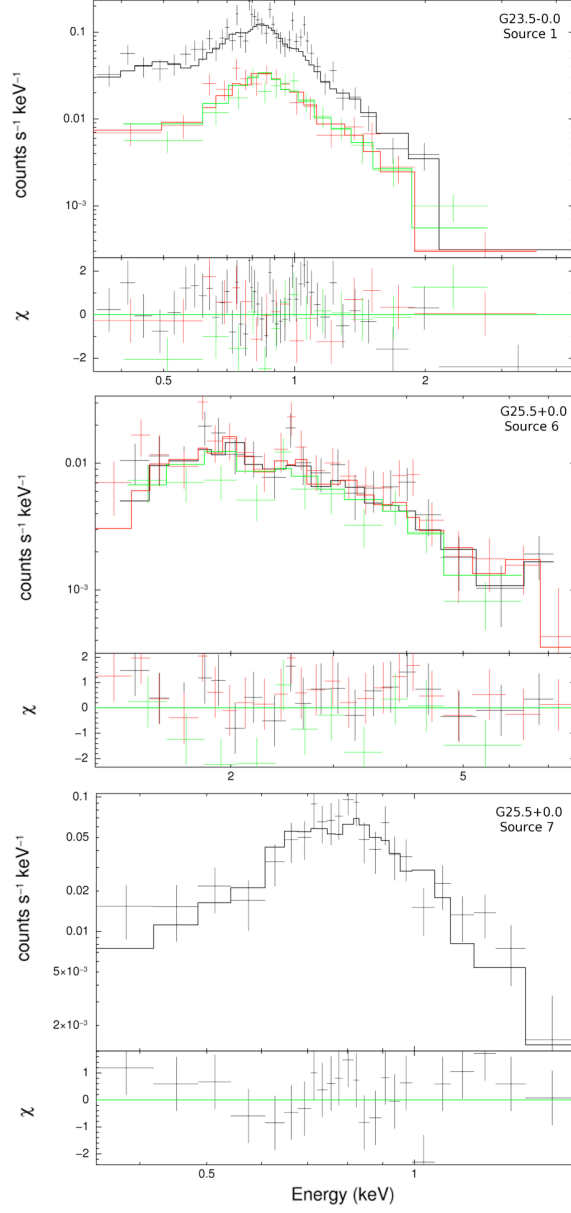


Fig. 3.— Absorbed *mekal* model fits to the EPIC spectra of Sources 1 (G23.5+0.1), 6 (G25.0+0.0), and 7 (G25.0+0.0). The best-fit parameters are given in Table 4.

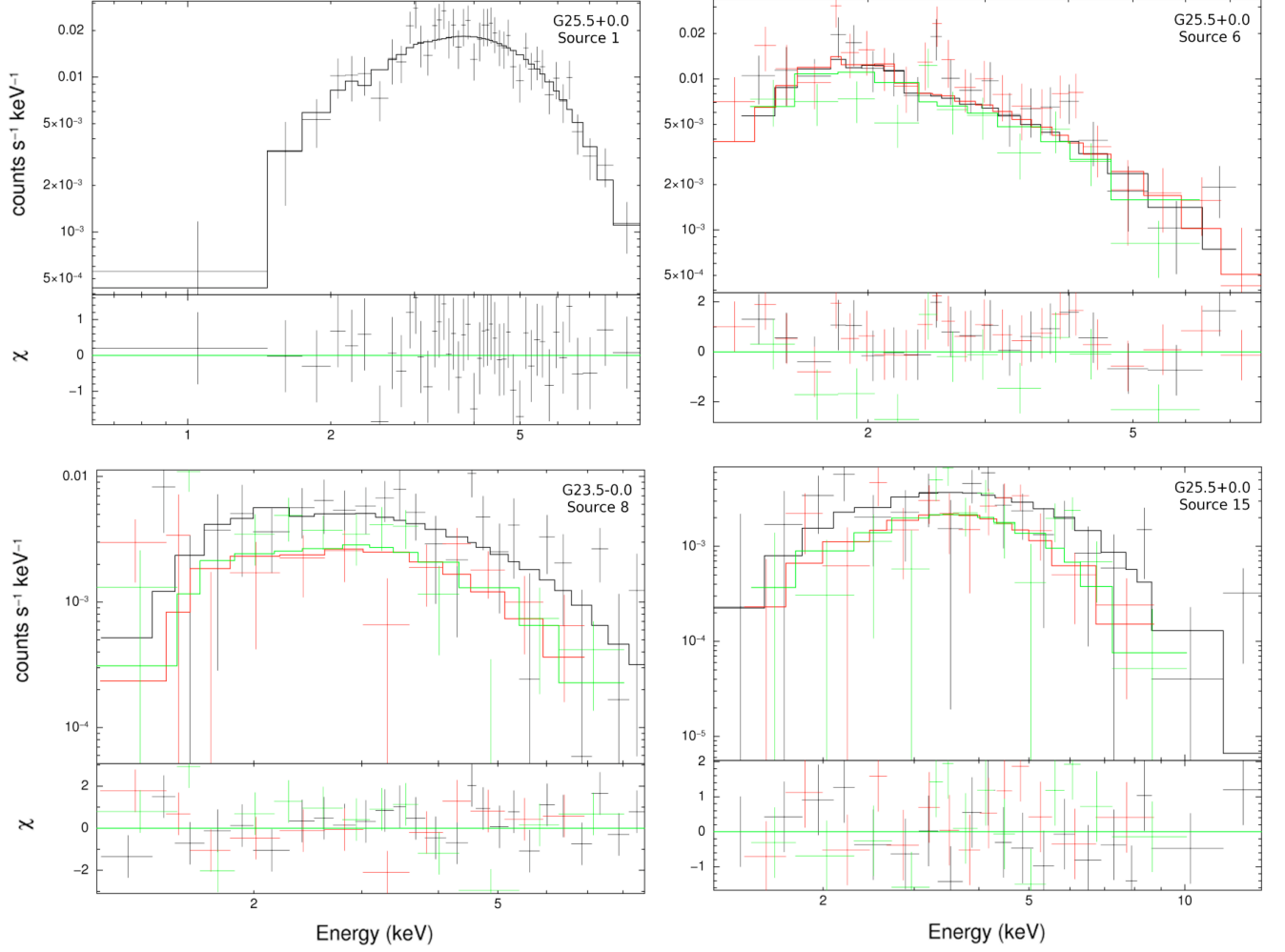


Fig. 4.— Absorbed PL model fits to the EPIC spectra of Source 8 in G23.5+0.1, and Sources 1, 6, and 15 in G25.5+0.0. The best-fit parameters are given in Table 5.

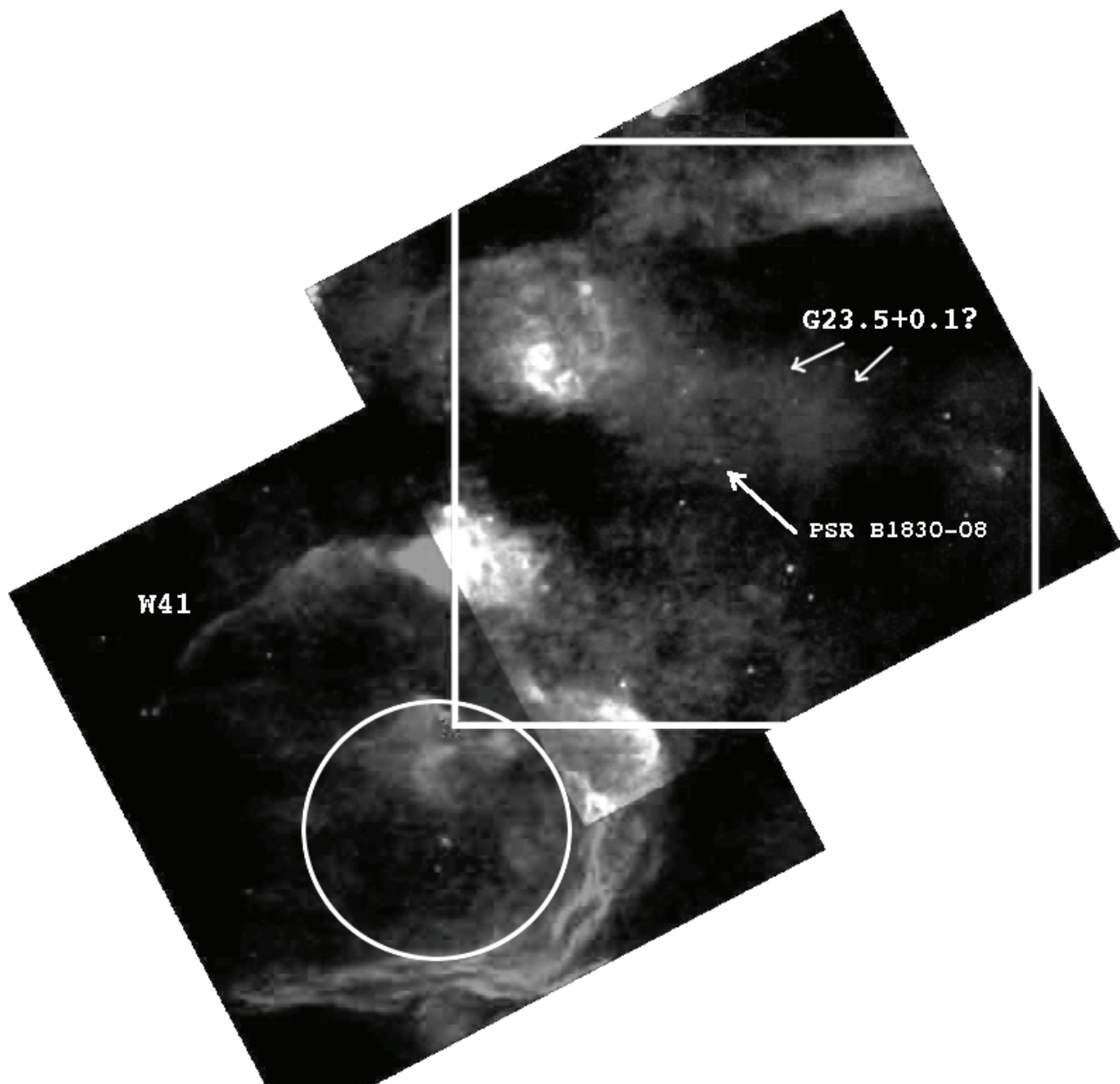


Fig. 5.— MAGPIS 20 cm composite image (1.4 GHz) showing the G23.5+0.1 and W41 fields together. The $32' \times 32'$ white box encloses the *XMM-Newton* EPIC FOV shown in Figure 1. The shell of SNR W41 is clearly seen. W41 appears to have no connection to PSR B1830–08 and surrounding it diffuse emission. The $r = 7'$ circle shows 1σ extent of the TeV source HESS J1834–087.

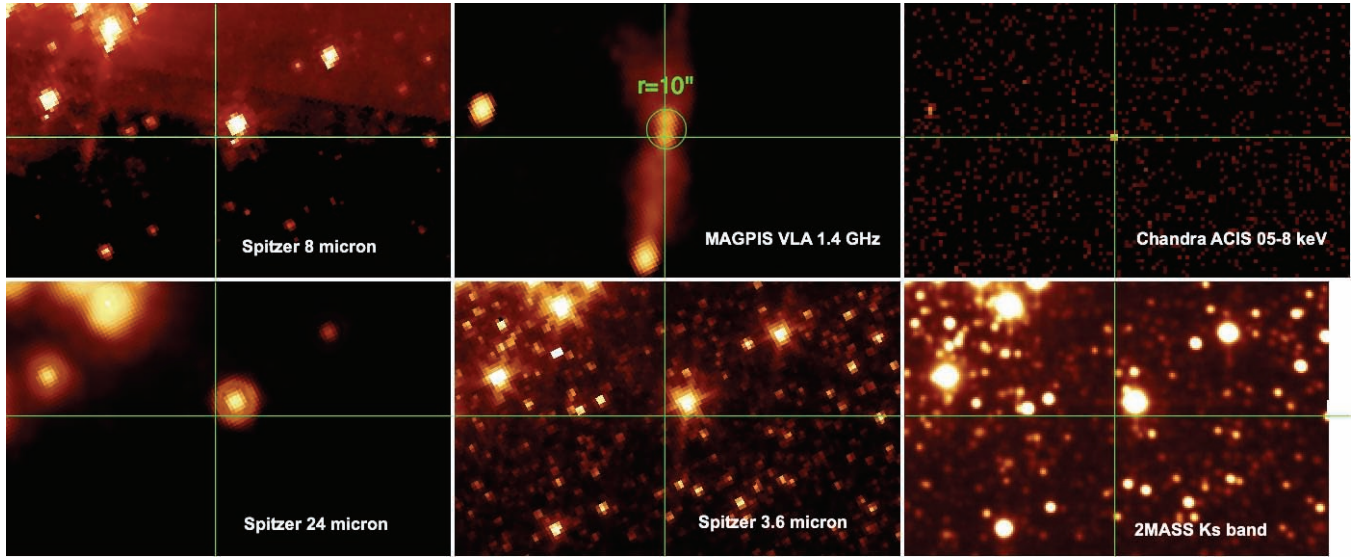


Fig. 6.— Radio source B (*XMM-Newton* Source 9 in the G25.5+0.0 field) at different wavelengths (see §4.3). The cross-hair is centered at the position of the *Chandra* source, CXOU J183751.62–064355.4, which is coincident with Source 9 (see top right panel).

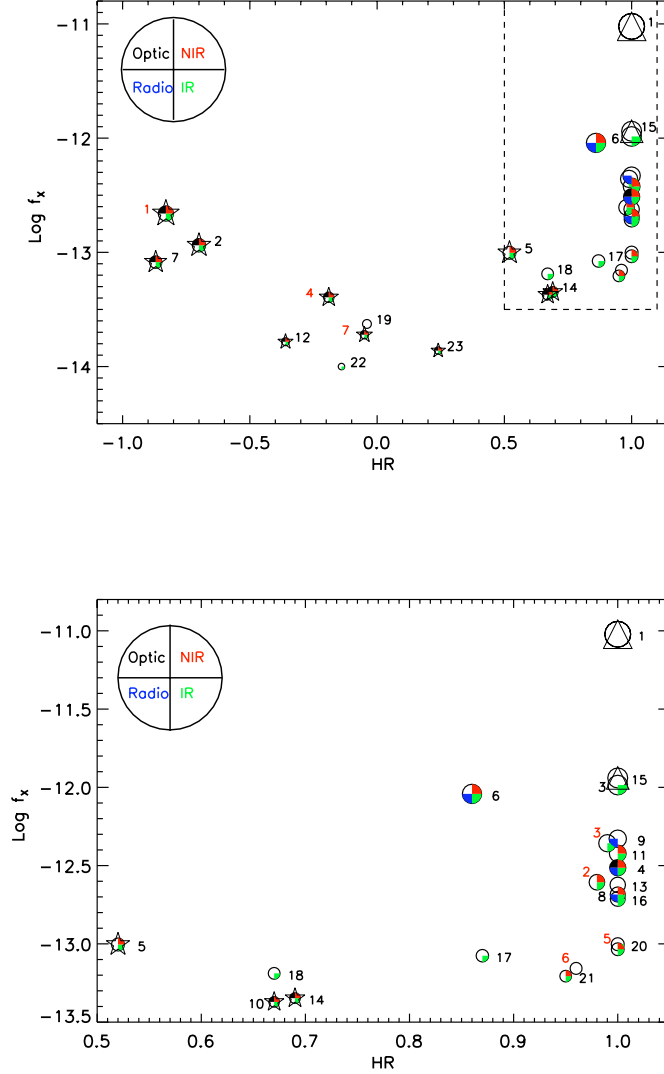


Fig. 7.— Logarithm of the observed 0.2–12 keV X-ray flux (f_X) versus hardness ratio (HR) for the X-ray sources detected in G23.5+0.1 and G25.5+0.0 fields (denoted by red and black numbers, respectively, in accordance with Tables 2 and 3). The bottom panel is the zoom-in of the upper right corner of the top panel (shown by the dashed lines). The sizes of the circles are proportional to $\log f_X$. The optical, 2MASS, GILMPSE, and radio detections are shown by filling the circle quadrants with different colors, according to the legend shown in the upper left corner. An empty (white) quadrant means nondetection in the corresponding wavelength range. Sources classified as foreground MS stars are additionally marked by the “star” symbol, while those classified as an AGN or PMS-star are marked by the “square” symbol. The young pulsar and the PWN candidate are marked by the “triangle” symbols. Classification of the sources shown by circles only (without additional symbols) is uncertain (see Tables 6 and 7).

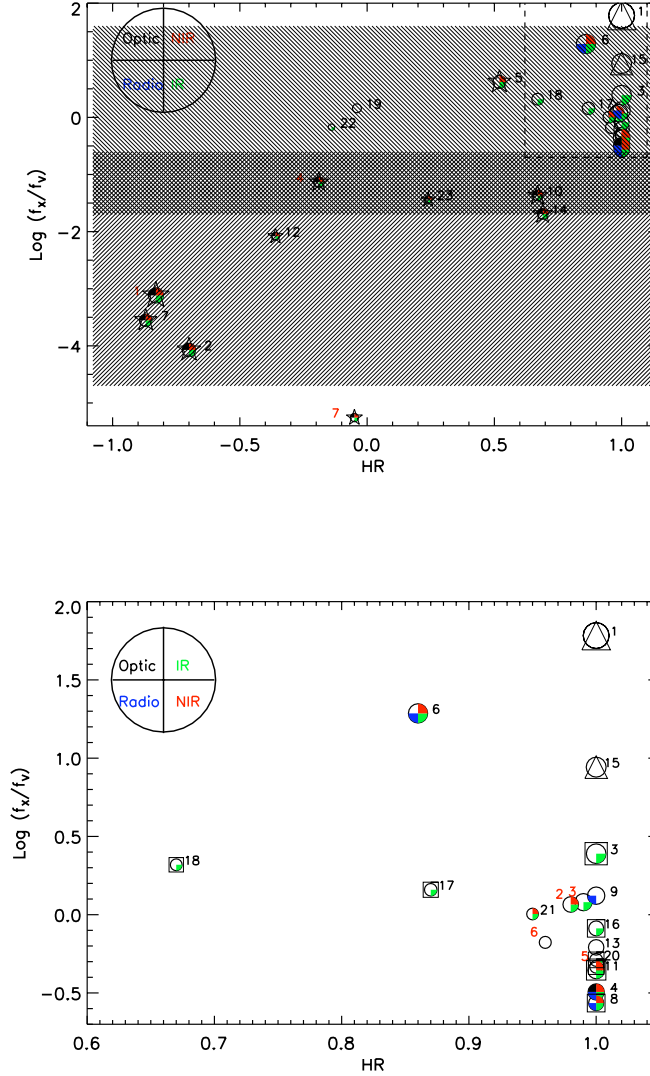


Fig. 8.— Logarithm of the X-ray to optical flux ratio ($\log f_X/f_V$) versus hardness ratio (HR) for the X-ray sources detected in G23.5+0.1 and G25.5+0.0 fields (denoted by red and black numbers, respectively, in accordance with Tables 2 and 3). The bottom panel is the zoom-in of the upper right corner of the top panel (shown by the dashed lines). The sizes of the circles are proportional to $\log f_X$. The optical, 2MASS, GILMPSE, and radio detections are shown by filling the circle quadrants with different colors, according to the legend shown in the upper left corner. An empty (white) quadrant means nondetection in the corresponding wavelength range. The circles with empty upper-left quadrants show lower limits on $\log f_X/f_V$. Sources classified as foreground MS stars are additionally marked by the “star” symbol, while those classified as an AGN or PMS-star are marked by the “square” symbol. The young pulsar and the PWN candidate are marked by the “triangle” symbols. Classification of the sources shown by circles only (without additional symbols) is uncertain (see Tables 6 and 7). The shaded regions correspond to main sequence stars (B-M classes; bottom region) and extragalactic sources (galaxies and AGNs; top region) according to the criteria defined by Maccacaro et al. (1988).

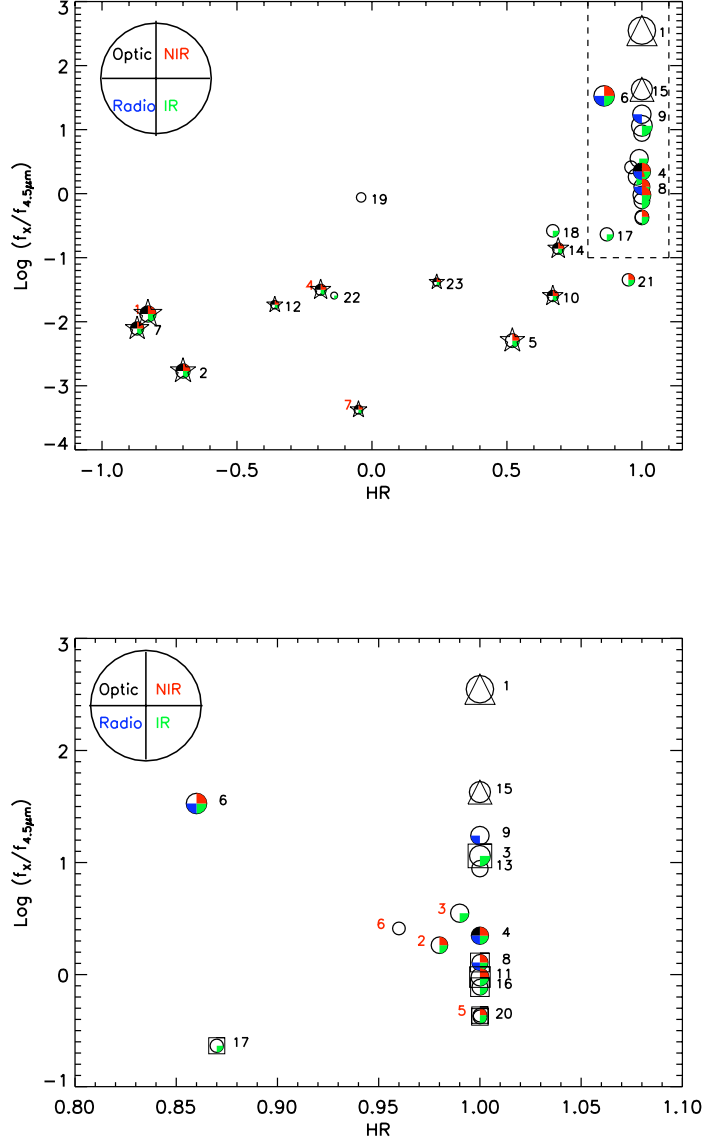


Fig. 9.— Logarithm of the X-ray to $4.5 \mu\text{m}$ flux ratio ($\log f_X/f_{4.5\mu m}$) versus hardness ratio (HR) for X-ray sources detected in G23.5+0.1 and G25.5+0.0 fields (denoted by red and black numbers, respectively, in accordance with Tables 2 and 3). The bottom panel is the zoom-in of the upper right corner of the top panel (shown by the dashed lines). Sizes of the circles are proportional to $\log f_X$. The optical, 2MASS, GILMPSE, and radio detections are shown by filling the circle quadrants with different colors according, to the legend shown in the upper left corner. An empty (white) quadrant means nondetection in the corresponding wavelength range. The circles with empty upper-right quadrants show lower limits on $\log f_X/f_{4.5\mu m}$. Sources classified as foreground MS stars are additionally marked by the “star” symbol, while those classified as an AGN or PMS-star are marked by the “square” symbol. The young pulsar and the PWN candidate are marked by the “triangle” symbols. Classification of the sources shown by circles only (without additional symbols) is uncertain (see Tables 6 and 7).